Perspective

Characterizing the Efficiency of Perovskite Solar Cells and Light-Emitting Diodes

Su-Hun Jeong,[1,8] Jaehyeok Park,[2,8] Tae-Hee Han,[3,8] Fei Zhang,[4] Kai Zhu,[4] Joo Sung Kim,[1] Min-Ho Park,[1] Matthew O. Reese,[4,*] Seunghyup Yoo,[2,*] and Tae-Woo Lee[1,5,6,7,*]

Metal halide perovskites (MHPs) are being widely studied as a light-absorber for high-efficiency solar cells. With efforts being made throughout the globe, the power conversion efficiency of MHP solar cells has recently soared up to 25.2%. MHPs are now being spotlighted as a next-generation light-emitter as well. Their high color purity and solution-processability are of particular interest for display applications, which in general benefit from wide color gamut and low-cost high-resolution subpixel patterning. For this reason, research activities on perovskite light-emitting diodes (LEDs) are rapidly growing, and their external quantum efficiencies have been dramatically improved to over 20%. As more and more research groups with different backgrounds are working on these perovskite optoelectronic devices, the demand is growing for standard methods for accurate efficiency measurement that can be agreed upon across the disciplines and, at the same time, can be realized easily in the lab environment with due diligence. Herein, optoelectronic characterization methods are revisited from the viewpoint of MHP solar cells and LEDs. General efficiency measurement practices are first reviewed, common sources of errors are introduced, and guidelines for avoiding or minimizing those errors are then suggested to help researchers in fields develop the best measurement practice.

INTRODUCTION

Metal halide perovskite (MHP)-based optoelectronic devices have a great potential to compete with the well-established optoelectronic devices such as silicon (Si), gallium arsenide (GaAs)-based solar cells, and organic light-emitting diodes (OLEDs). Three-dimensional (3D) MHPs have an ABX_3 perovskite structure where A is an organic cation (e.g., methylammonium [MA] $CH_3NH_3^+$, formamidinium [FA] $CH(NH_2^+)$, or an alkali-metal cation such as Cs^+), B is a transition-metal cation (e.g., Pb^{2+}), and X is a halide anion (Cl^-, Br^-, or I^-). The optical and electrical properties of MHPs are easily tunable by substituting cations and anions. MHPs are solution-processable semiconductors with unique optical and electrical properties due to the combination of a high absorption coefficient ($CH_3NH_3PbI_3$: ~10^4 cm^{-1}-10^5 cm^{-1} for photon energy ranging 1.5 eV–3.0 eV)[1] that is higher than that of Si and long carrier diffusion length. The photogenerated carrier profiles depend on the absorption coefficient of the absorber, and the high absorption coefficient of MHPs, along with long carrier diffusion length, makes it possible to be thin, typically less 500 nm.[2–4] The fundamental origin of these unique electronic and photophysical properties have been found to be the unique atomic electronic configuration of

Context & Scale

Metal halide perovskite (MHP)-based solar cells and light-emitting diodes (LEDs) have shown a great potential to compete with the conventional optoelectronic devices such as silicon, gallium-arsenide-based inorganic solar cells, and organic LEDs. MHPs have been widely studied as a light-absorbing material for high-efficiency solar cells due to their high charge-carrier mobility and direct band gap leading to large absorption coefficient. Also, MHPs provide benefits of wide color gamut and low fabrication cost for display applications due to their high color purity and solution processability.

There are features specific to MHP-based solar cell and LED devices that make accurate measurement of their device efficiency challenging or at least tricky. In the context, optoelectronic characterization methods and common sources of errors are reviewed, and accurate measurement guidelines for device efficiencies in a viewpoint of MHP-based solar cells and LEDs are suggested. The guidelines would improve the reliability in the uprising research on MHP-based solar cells and LEDs, helping researches in the fields develop the best measurement practice.

Pb and symmetry of MHPs (the lone pair Pb 6s and the inactive Pb 6p orbitals, plus strong spin orbit coupling induced by its heavy atomic mass).[5] The conduction band minimum (CBM) of MHPs mainly forms from Pb 6p states, and the valence band maximum (VBM) consists of antibonding states of Pb 6s and I 5p orbitals. The unique combination of electronic and structural (symmetry) properties in MHPs renders not only direct band gap but also p-orbital-to-p-orbital optical transition (absorption), which is ideal for a good light absorber and light-emitter. From the electronic configuration, MHPs also possess advantages of small effective mass for both hole and electron and less non-radiative recombination due to their defect-tolerant electronic characteristics, and therefore have an exceptionally long carrier lifetime (>1 μs) and diffusion length (>1 μm).[3–5]

In recent years, use of MHPs has been increasingly extended to the field of light-emitting diodes (LEDs). Their high color purity with narrow full-width-half-maximum (FWHM) of luminescence makes MHPs attractive for future display applications.[6,7] Luminescence band shape can be generally related to the vibrational motion of crystal lattice and/or molecules of the electronic ground state and excited states (i.e., electron-phonon coupling).[8] Certain high-frequency molecular vibration modes in organic molecules result in strong electron-phonon coupling, which leads to a large equilibrium offset between ground and excited states, thereby broadening the emission and incurring a large Stokes shift.[8] For example, the molecular torsional mode of the conventional organic emitter N,N'-Bis (3-methylphenyl)-N,N'-diphenyl-benzidine (TPD) leads to a large Stokes shift and broad emission with Poisson progression over an effective mode of 158 meV (Huang-Rhys factor, S:0.87).[9] The electron-phonon coupling in MHPs, which mainly stems from longitudinal-optical phonon of metal-halide vibration mode (~60 meV, S:0.6),[10] is less than in organic luminescent materials, resulting in a smaller Stokes shift and narrower emission band width than those of organic materials used in OLEDs.[8,10]

The electroluminescence (EL) efficiency of perovskite LEDs (PeLEDs) has been dramatically improved in a relatively short period; the highest external quantum efficiency (EQE) over 20% has been reached, which is comparable to those of phosphorescent OLEDs.[11–13]

The certified power conversion efficiency (PCE) of perovskite solar cells (PeSCs) have reached 25.2%.[14] Accurately and precisely measuring the efficiency of solar cells is one of the basic procedures in photovoltaic labs worldwide. International certification labs serve as the custodians of the record efficiencies, which publish semi-annually in *Progress in Photovoltaics*[14] and more recently have been compiled with detailed information in an interactive graph available online.[15] It is important, however, for research and development labs to be able to measure similar values as a certification lab. While there is not an analogous certification infrastructure for LEDs, the same general principle applies of wanting comparable performance measurements between labs.

While the methods for characterizing PeSCs and PeLEDs may largely be taken from other portions of the wider (thin film) solar cell and (organic) LED communities, this does not mean that they are uniformly and well-practiced; furthermore, some of the material properties of perovskite optoelectronic devices require additional care when performing measurements. The ion migration and potentially related hysteretic effects in perovskite devices in particular can have strong effects on elements such as scan rate and sweep directions in both PeSCs and PeLEDs. In the case of PeLEDs, the optoelectronic measurement methods can be taken largely from those used for

[1]Department of Materials Science and Engineering, Seoul National University, 1 Gwanak-ro, Gwanak-gu, Seoul 08826, Republic of Korea

[2]School of Electrical Engineering, Korea Advanced Institute of Science and Technology (KAIST), 291 Daehak-ro, Yuseong-gu, Daejeon 34141, Republic of Korea

[3]Division of Materials Science and Engineering, Hanyang University, Seoul 04763, Republic of Korea

[4]National Renewable Energy Laboratory (NREL), 15013 Denver West Parkway, Golden, CO 80401, USA

[5]Research Institute of Advanced Materials, Seoul National University, 1 Gwanak-ro, Gwanak-gu, Seoul 08826, Republic of Korea

[6]Nano System Institute (NSI), Seoul National University, 1 Gwanak-ro, Gwanak-gu, Seoul 08826, Republic of Korea

[7]Institute of Engineering Research, Seoul National University, 1 Gwanak-ro, Gwanak-gu, Seoul 08826, Republic of Korea

[8]These authors contributed equally

*Correspondence:
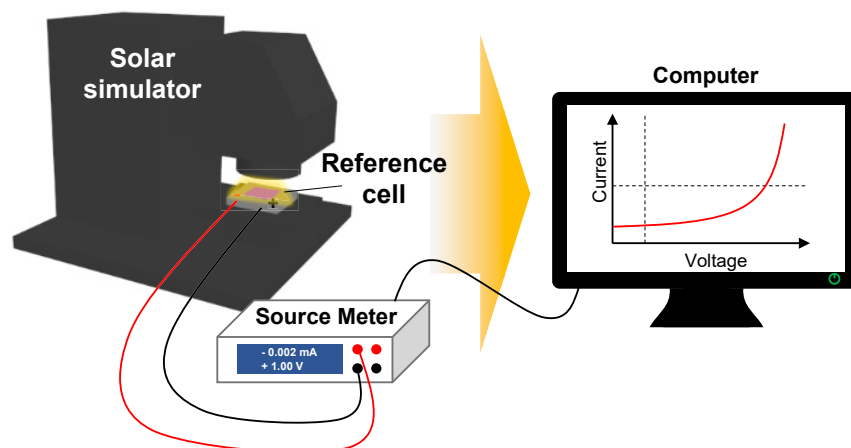matthew.reese@nrel.gov (M.O.R.), syoo@kaist.ac.kr (S.Y.), twlees@snu.ac.kr (T.-W.L.)

https://doi.org/10.1016/j.joule.2020.04.007

Figure 1. Schematic Illustration of PCE Characterizing Methods for PeSCs

OLEDs[16] because their planar configurations are essentially the same. Nevertheless, some properties specific to PeLEDs can make the measurement more prone to errors. For example, much narrower EL spectra inherent to PeLEDs can render their angular characteristics to be different from that of Lambertian,[17,18] which has often been assumed for bottom-emission-type OLEDs having a no- or low-microcavity effect. Different ratios of the current efficiency (CE) to EQE values reported, even for the identical device geometry combined with the same emitters, suggest that there are group-to-group variations in treating the angular spectral characteristics in their EQE estimation. Hysteretic behavior is also an important factor that can make it tricky to precisely characterize the metrics of both PeSCs and PeLEDs, although ion migration may be exploitable in memristors and synapse-mimicking devices.[19,20] Effect of parameters like scanning rate and bias-sweep direction must be taken into account carefully.[17,21] Of course, it will also be important to identify the material set and device architectures that are relatively robust against hysteresis.[22] As the efficiency records of PeSCs and PeLEDs are continually increasing over time, it is essential to establish standardized guidelines to characterize efficiencies for both PeSCs and PeLEDs. Here, we first present a brief introduction to efficiency measurement methodologies for PeSCs and PeLEDs along with definition of key terms and discussion on common sources of errors in perovskite-based devices. We then suggest practical guidelines for avoiding or minimizing those errors to ensure precise estimation of the efficiencies in those devices.

CHARACTERIZING THE EFFICIENCY OF PEROVSKITE SOLAR CELLS

Three pieces of equipment are required at minimum for reasonable quality measurements: a solar simulator, a quantum efficiency (QE) measurement tool, and a calibrated reference cell (Figure 1). A fourth piece of equipment, a spectrometer to capture the lamp spectrum, is required for the highest quality measurements. This section of the paper will describe our view on the equipment, considerations, and procedures to encourage accurate and precise efficiency measurements for hybrid perovskite solar cells in a manner accessible to R&D labs.

Characterization Tool: Solar Simulator, Quantum Efficiency Measurement Tool, Reference Cell
Solar Simulator
To begin, solar cells are measured in relation to a standard reference spectrum with standard test conditions. For non-concentrating or tracking terrestrial applications,

the reference spectrum is AM1.5G (Figure S1A).[23] The "AM" stands for "air mass" and 1.5 is how many thicknesses of the atmosphere have been traversed; one is traversed when the incident light travels normal to the atmosphere. The 'G' stands for global tilt—used to account for "flat plate" (i.e., systems intended to operate at 1 sun). In this spectrum, there are both direct and diffuse components compared to AM1.5D, which is solely the direct portion of the spectrum, which is appropriate for concentrating systems that must track the sun's motion, because as concentration levels increase, the collection angle of light is limited, which decreases the contribution of the diffuse component. While the reference spectrum is somewhat arbitrary, as the spectrum even at a single location changes with time, it is meant to simulate a mid-latitude spectrum (e.g., the United States) around noon on a clear day. For the interested reader, a nice solar spectrum calculator found online can be used to illustrate the variations.[24] While somewhat arbitrary, the reference spectrum has very important effects on final measurements as will be seen below. Standard test conditions (STCs) specify an irradiance of 1 sun to be 1 kW m^{-2} (100 mW cm^{-2}), which tends to be present at most locations only on a sunny day around noon, as well as a nominal operating cell temperature of 25°C. While 25°C is close to room temperature, cells can heat up quickly to much higher than this value (>40°C is readily possible) without some sort of active cooling (e.g., a fan or water-cooled plate) integrated into a solar simulator. The choice of these conditions can be understood, in addition to the appealing roundness of the numbers, because most solar cells (c-Si especially) are more efficient at lower temperatures and higher intensity solar irradiance.

Solar simulators are typically sold with a three-letter class system. In order, they indicate the quality of the spectral match, spatial uniformity, and temporal stability. Table S1 defines what classes A–C mean for each type. The spectral quality is often the biggest focus of many groups. To understand this, Figure S1A shows a representative spectrum of a class A spectrum xenon-lamp-based simulator with its AM1.5G filter set compared to the actual AM1.5G reference spectrum. To establish that this spectrum is indeed class A, after measuring the simulator's spectrum, one would integrate the irradiance of 100-nm-wide bins from 400–900 nm and one 200-nm-wide bin from 900–1,100 nm of the simulator and compare it to the integrated values for the reference spectrum. To be a class A spectrum requires that each bin be within ± 25% of the integrated reference spectrum. While a simulator's class is defined by its worst bin, a bin may have regions that are significantly lower or higher irradiance than the bin's average. This binning with integrated irradiance thereby makes the spikes associated with many lamp spectra acceptable. Furthermore, irradiance values are unspecified at <400 and >1,100 nm. Simulators that have a bin worse than class C are sometimes specified as class X. It is possible to generate a relatively inexpensive solar simulation source from a lightbulb that is technically a class X simulator but has high quality matching in the region of interest to higher band-gap technologies.[25] It is also worth noting that purchasing a simulator of a particular class (e.g., AAA) should be able to achieve its designated class; however, if it has not been calibrated, it is typically not performing at this level. Lamp spectra can vary with time, although manufacturers often try to take this into account when designing their filters over a specified lamp life. More significantly, whenever a bulb is changed, the spatial uniformity must be recalibrated. According to International Electrotechnical Commission (IEC) 60904-9,[26] the spatial uniformity should be measured in a minimum grid of 8 × 8 points across the designated area. This can be done by moving a small area Si cell held parallel to the measurement plane, although more sophisticated apparatuses exist as well, including multiple diode arrays or cells on motion stages. It is worth emphasizing that the spatial uniformity

specification is over a designated area. Many groups have simulators with much larger designated areas than their test cells. To minimize the effects of spatial uniformity, two approaches can be taken. The most straightforward is to measure each cell in the exact same location—if multiple cells are on a substrate, the substrate is shifted between measurements. The second approach is to measure substrates in a fixed location relative to the lamp and calibrate the relative variation between cell locations on the substrate. In the event that a cell is larger than the uniformity, other methods can be used.[27] Changes in irradiance with time (temporal stability) are often associated with the power supply and bulb age (older bulbs may start being unstable). To remove these variations, a monitor diode can be measured simultaneously over the course of an efficiency measurement of a test cell. This can then establish if the irradiance during a particular measurement was, for example, 1.01 sun. Assuming linearity (which can be measured for a particular cell or configuration), the measured current can then be renormalized back to a 1-sun value.

Standard test conditions dictate that efficiencies should be at 1-sun intensity. This is typically established in the case of simulators with divergent sources by adjusting the separation between the lamp and sample. For simulators with collimated sources, the intensity is relatively constant with separation, so instead the lamp power is adjusted to achieve 1-sun intensity, which may be maintained by feedback to a monitor diode. While this can achieve a fairly constant irradiance, the spectrum can shift somewhat with lamp power changes. A simulator is set to its 1-sun intensity immediately prior to sample measurement using an appropriate reference cell (discussed below) by making adjustments to the simulator as appropriate to achieve the 1-sun short-circuit current of the reference cell.

It is well-known that changing the irradiance can lead to different recombination dynamics as the open-circuit voltage increases logarithmically with the ratio of photocurrent to dark (recombination) current. Fill factor has a more complicated relationship, with potential changes in series and shunt resistance, as well as ideality factor. This is why the highest reported efficiencies have been at high concentrations for III-V cells.[6] In the absence of complications with keeping cells at constant temperature and series resistance losses from joule heating, solar cells should ideally be more efficient at higher irradiance with higher V_{OC} measured. Altering carrier dynamics (e.g., the onset of bimolecular recombination), however, can lead to a reduction in fill factor with increasing irradiance. Since there is an optimum concentration value for each cell, standard test conditions should be performed as close to 1 sun as possible rather than an arbitrary intensity and then normalizing to 1 sun. This allows a direct comparison within a technology as well as between technologies.

Quantum Efficiency Measurement Tool
The external QE of a solar cell is a measure of the likelihood of whether photons of a particular wavelength can be harvested and converted to current. This ultimately is used to establish the spectral responsivity of a cell. Figure S1B shows several QEs of different band-gap perovskite cells. Some groups use a purchased turn-key system for this; others will make their own using a monochromator, chopper, lock-in, preamp, and reference cell. While many will do a "dark" QE measurement in which the only intentional light incident on the cell is the very weak, monochromatic light (< 0.01 sun), a white-light-biased measurement is preferable, in which a "DC light biases the cell closer to realistic operating conditions, with the chopped monochromatic light representing only a small perturbation. This means that what is actually measured is a differential spectral responsivity rather than a direct spectral responsivity. Samples measured without a light bias can artificially be affected by trap

states, which a light bias can readily fill.[28,29] Similarly, surface passivation can be wavelength dependent.[28] "Well-behaved" cells might be considered only modestly non-linear over a wide range of intensities without great sensitivity to chopping frequency—although it is worth noting that DC bias light can mitigate low response times.[29] Furthermore, non-linearity by itself is not an exceptional case for solar cells with even Si cells documented to exhibit non-linearities.[28,30] Sublinear behavior can occur for a number of reasons including field dependent charge collection, which collapses with increasing irradiance and decreasing diffusion lengths.[28,30] Intensity-dependent QE has also been used to study recombination mechanisms (e.g., bimolecular recombination, field effects, and contact layers) and even correlate them with fill factor.[31] Supralinear behavior can be observed for cells in which the series resistance limits J_{sc}.[30] Edge effects have been correlated to both sub- and supralinear behavior.[30] While dark QE can lead to errors as large as 100% in J_{sc}, the lowest error is counterintuitively obtained at irradiances less than 1 sun.[30] For samples that are non-linear, the non-linearity can be represented as $J_{SC} = c \times I^{\gamma}$, where I is the irradiance, c is a constant, and γ is a measure of the non-linearity ($\gamma = 1$ is linear). The formula $J_{DC\ Bias} = \gamma^{\gamma/(\gamma-1)} J_{SC,\ 1\ sun}$ can be used to calculate the correct bias light irradiance as measured by the measured device current density ($J_{DC\ Bias}$). For mildly non-linear behavior (i.e., $0.9 < \gamma < 1.1$), this minimum in error corresponds to EQE measurements performed with a light bias of ~1/e of the 1 sun irradiance.[30] For devices with much greater non-linearity, the bias light intensity should be adjusted to minimize the error.

EQE is a measure of the fraction of the incident photons that are converted to photocurrent, whereas internal quantum efficiency (IQE) is a measure of the fraction of absorbed photons that are converted to photocurrent. In general, QE (EQE or IQE) can be affected by light harvesting and charge collection, depending on the actual materials and structures used in a device stack. The non-ideal QE can thus be attributed to optical loss and/or electrical loss. The optical loss primarily consists of the loss from reflection and parasitic absorption from various transport or contact layers. In a study[32] using 1.55-eV perovskite absorber as an example, detailed modeling coupled with experimental data shows that the maximum J_{sc} (27.23 mA cm^{-2} based on the 1.55-eV band gap) can be reduced to 21.61 mA cm^{-2} from the reflection loss of 2.48 mA cm^{-2} (9.1%) and parasitic absorption loss of 3.14 mA cm^{-2} (11.5%) from transparent conducting oxide (TCO) and the contact layers. Using an antireflection coating is a common way to reduce the reflection loss—reducing reflection losses by more than ~3%–4% absolute over a wide wavelength range is challenging.[33] The parasitic absorption loss can also be reduced by using thinner transport layers or using alternative materials with less absorption in the spectrum range relevant to the absorber layer. Electrical loss primarily results from surface recombination at front or back contacts, short diffusion length associated with poor transport and/or carrier lifetime, and resistive loss from series and shunt resistances. In the same study,[32] it was shown that the electrical loss could account for 17.7% loss of the power output. It is worth noting that the electrical loss is related to charge collection, which could be affected by the voltage bias conditions. Thus, QE should be measured at short-circuit condition to avoid voltage-bias-induced current, especially for low-quality devices.

For QE measurement, it is worth noting that the chopping frequency should be slow enough to not affect charge collection and not be at the power line frequency or a multiple thereof (prime numbers are a good choice; e.g., 37 Hz). The DC light source may be at the line frequency and does not need to have a class A spectrum. Both absolute and relative QEs can be measured. An absolute QE (e.g., the different

band-gap perovskite cell QEs in Figure S1B) requires that the entire beam from the system be focused within the device area, such that a known intensity is striking the sample. A relative QE uses a larger spot than the sample, as in the Si reference cell QEs shown in Figure S1B. Measuring the QE yields not only important information about a device's behavior (e.g., absorption depth, optical losses, band gap), but it is also used to establish the spectral mismatch factor and, in the case of an absolute QE, can be integrated to verify current-voltage (IV) measurements.[34] When reporting results, QE and IV data of the *same cell* should be presented together rather than cherry-picking "representative" data. This is especially important for perovskite systems in which the composition and hence band gap may be somewhat altered between samples.

Calibrated Reference Cell

A calibrated reference cell with known QE and 1-sun current is also required for solar simulations. For a group focusing on research at a single band gap, the reference should have as similar a band gap as possible. For a group exploring numerous band gaps, either multiple reference cells should be used or an Si reference with multiple filter sets should be employed. A reference cell should be in a package that is light impervious such that no stray light will reach the side or back of the reference. A reference cell should be stable over time. Even Si reference cells are technically supposed to be recalibrated once a year. One of the certification labs can be used for this service. Similarly, a reference cell for QE measurements is important.

Avoiding Measurement Discrepancy and Errors
Spectral Concerns

Once a user has representative QE information about the cell under test, the reference cell, and the lamp spectrum, a spectral mismatch factor may be determined. First, the QE, η_{QE}, is transformed into a spectral responsivity, S, using Equation 1,

$$S_x(\lambda) = \frac{q\lambda}{hc}\eta_{QE,x}(\lambda) \qquad \text{(Equation 1)}$$

where the subscript, x, is used to indicate if the QE is from the reference cell or test cell, q is charge quantity, h is Planck constant, and c is the speed of light in vacuum. Then, a series of four convolutions are performed to balance the currents that would be measured by either the reference cell or test cell under either the reference spectrum or lamp spectrum (represented as $I_{x,y}$ below) to calculate the spectral mismatch factor, M,

$$M = \frac{\int_{\lambda_1}^{\lambda_2} E_{Ref}(\lambda)S_{Ref}(\lambda)d\lambda}{\int_{\lambda_1}^{\lambda_2} E_{Ref}(\lambda)S_{Cell}(\lambda)d\lambda}\frac{\int_{\lambda_1}^{\lambda_2} E_{Lamp}(\lambda)S_{Cell}(\lambda)d\lambda}{\int_{\lambda_1}^{\lambda_2} E_{Lamp}(\lambda)S_{Ref}(\lambda)d\lambda} = \frac{I_{Ref,1\ sun}}{I_{Cell,1\ sun}}\frac{I_{Cell,Meas}}{I_{Ref,Meas}} \qquad \text{(Equation 2)}$$

where E_{Ref} is the irradiance of the reference spectrum (e.g., AM1.5G), E_{Lamp} is the irradiance of the lamp, S_{Ref} is the spectral responsivity of the reference diode, and S_{Cell} is the spectral responsivity of the test cell. These four integrals are presented graphically in Figure S3 to try to illustrate what the spectral mismatch factor is doing. This is adapted from a recent book chapter, which has an expanded discussion.[35] The change from QE from spectral responsivity is illustrated, as well as the effect this has with the integrated spectrum. A cell has an increasingly weighted response to photons near its band edge. This is important to consider when choosing a reference cell for a particular test cell. The spectral mismatch correction has the greatest influence on the current (i.e., J_{sc}), with a correction being directly applied to each current point in the current-voltage curve. This has a second order effect on the fill factor, with generally very limited changes to the open-circuit voltage. Even though
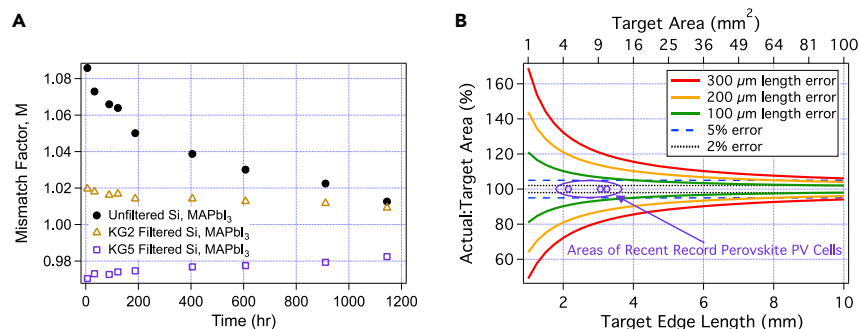
Figure 2. Spectral Mismatch and Length (Area) Concerns

(A) Spectral mismatch factor, M, versus time calculated for a Si reference cell with either no filter, a KG5, or a KG2 filter relative to a MAPbI$_3$ cell for a class A filtered xenon-lamp-based solar simulator.
(B) Length (area) errors calculated for a square cell with a side of target length. These errors can begin to dominate other sources with even minor (mis)measurements. Recent perovskite records have all been for small area cells, illustrating the importance of area measurement.

a cell exhibits significant wavelength dependence over its collection range, class A spectra tend to minimize voltage effects.

Before using a simulator, a user will typically set the 1-sun intensity based off their reference cell's known calibrated current ($I_{Cell, Meas}$). This value is how much current the reference should generate under the reference spectrum. In doing this, two of the integrals should cancel one another (reference spectrum*reference cell and lamp*reference cell). When the test cell is measured, $I_{Cell,Meas}$ is represented by the integral of lamp and test cell. This needs to be transformed into the current that would be produced if the test cell were exposed to 1-sun intensity under the reference spectrum (the last integral, $I_{Cell,1 sun}$). To transform the measured current under the lamp spectrum, one simply takes the measured cell current and divides by M (assuming that the simulator was actually set to exactly 1-sun intensity on the reference diode).

Ideally, M should be as close to unity as possible. In examining the integrals, one sees that there are two hypothetical ways to guarantee a mismatch factor of unity. One is to have a lamp spectrum that is identical to the reference; the other is to have a reference cell with identical spectral response to the test cell. In reality, neither will be possible. While having a well-matched (i.e., class A) spectrum is a good start to minimizing spectral errors, by itself it is not enough. Some researchers put an excessive amount of value in the spectral class of a simulator and then pay little attention to making sure they have a reference cell that has a similar spectral response to their test devices. A poorly matched reference cell will respond to different (extra or fewer) portions of the lamp spectrum than the test cell, making the measurement more sensitive to differences between the lamp and reference spectrum. This is illustrated in Figure 2A, where MAPbI$_3$ is compared to an unfiltered Si reference cell (a poor choice). In general, it is significantly less expensive and easier to have a reference cell that is well-matched to the test cell than matching the lamp to reference spectrum (remember class A means $\pm$ 25% *integrated* mismatch per spectral bin). The easiest way to do this for any technology is to have a stable, packaged representative cell certified and use this as a reference. If possible, a group can make and package one of their cells for measurement by a certification lab and use it on occasion for calibrations. The next best way for groups that might want to explore different band gaps is to have a packaged Si reference cell

calibrated with a series of bandpass filters. Some representative filters and what they do to an Si cell are shown in Figure 2A; inexpensive bandpass filters (e.g., Schott Glass BG- or KG-series colored glass filters) can be appropriate for standard perovskite band gaps. GaAs references can also be purchased, which are relatively well matched to MAPbI$_3$. It is worth noting that reference cells should ideally be packaged in a manner that will minimize backside collection, reflections, and light piping (waveguiding through a substrate to a device).

For the best measurements, the lamp spectrum at the time of the measurement should be known. Lamp spectra can change over a bulb's lifetime. In the case of popular xenon arc lamps, this is a result of deposition of the electrode over time onto the quartz envelope of the lamp as a thin layer screens out short (blue) wavelengths. Initially, the lamp will uniformly pass the generated light. Over time, the lamp spectrum transitions from being blue rich to red rich. Measuring the lamp spectrum allows the diligent user to measure these shifts. In the case of inappropriate choice of a reference cell (poorly matched spectral response), the changing lamp spectrum for even good simulators can result in large shifts in the spectral mismatch factor, M (Figure 2B). Careful choice of the reference cell can mitigate this effect. For reasonably good measurements, having representative early-life and end-life spectra of the lamp can allow a group to establish the limits of this effect, although it is worth noting that different bulbs and different filter sets from the same manufacturer can result in somewhat different spectra (Figure S3). This information should be used to inform the potential magnitude of spectral errors rather than trying to ascribe absolute values. It is worth noting that measuring the lamp spectrum in well-calibrated units of W m^{-2} nm^{-1} requires carefully calibrating the spectrometer. Typical inexpensive USB spectrometers out of the box have well-calibrated wavelengths, but not intensity.

These spectral shifts also can have important implications on stability measurements. Apparent changes in efficiency can be either masked or exacerbated, with bulb changes leading to abrupt shifts in data. While xenon-arc bulbs are well-loved by scientists seeking a class A spectrum, spectral sensitivity on stability is hard to know for a technology that is rapidly exploring changes to not only its absorber formulation but architecture. Likely, if intensity is being monitored with an appropriately matched reference cell, the spectral changes over a single lamp's lifetime will have minor effects on stability. Some may choose to use alternate light sources that might be cheaper and/or more stable over time (e.g., metal halide, sulfur plasma, or LEDs), but ultimately there is not a single "correct" source because the spectral sensitivity on stability is not well understood. In practice, each architecture will have to be individually examined. It should be noted that UV-rich or -poor light sources may play a role in certain systems (e.g., transport layer trap filling and/or photocatalytic behavior). The authors are unaware of clear evidence that can balance the effects generally for perovskite systems of spectral match, spatial uniformity, and temporal stability—setting up stability systems is always a compromise of these three aspects because cost plays a role over long times and large areas. Following recommended practices like those proposed by Reese et al. for the organic photovoltaic community,[36] in which a minimum of information always accompanies stability measurements including the lamp spectrum, can at least help the community understand the measurement conditions.

Area Concerns

Perhaps most surprisingly, one of the biggest sources of errors historically in measuring emerging photovoltaic technologies has been associated with what

should be straightforward for all labs: area measurement. Research groups tend to make small cells for a variety of reasons including lack of uniformity, pinholes, attempting to get larger current densities and fill factors through poorly optimized front contacts, and the desire for statistics on small substrates (25 × 25 mm²). There are several approaches to cell layouts. One uses a "crossbar" geometry in which there is a patterned transparent contact, and a metal contact is evaporated through a shadow mask. In this case, the cell area should be the overlap between the transparent and metal contact.

However, it has been shown that conductive transport layers can lead to large (>60%) errors for small devices[37] from collection outside of the metal and transparent contact overlap region. Other groups will create "island" back contacts on an unpatterned transparent contact. This addresses collection from a conductive transport layer in contact with the transparent contact, but not from any conductive layers at the back. Additionally, it is worth noting that many groups who use shadow masks do not measure the area of a device each time, but rather assume that the metal area is well known. Shadow masks lead to imperfect edge definition with the potential for tens of microns to >100-µm spillover at each edge.

Furthermore, the opening of the shadow mask changes in size with the buildup from many depositions. Rotating a substrate during the deposition tends to improve the contact but exacerbates area definition problems. Even using a calibrated optical microscope to measure the area of a sample with shadow mask deposited contacts can lead to discrepancies for the location of a metal edge—different users may make different judgement calls that can result in >100-µm differences in lengths. Furthermore, it has been demonstrated that when laterally conductive transport layers are utilized, carrier collection can occur millimeters away from the metal contact, but even when low lateral conductivity transport layers are used, significant collection can still be observed hundreds of microns away from the metal's edge.[37]

Figure 2B highlights the potential error associated with small area devices that do not have carefully defined areas with some of the more recent device areas for certified record perovskite cells. For samples that are not "mesa isolated" (one contact and absorber is etched down to the other contact), an "aperture" is used to define the device area during the efficiency measurement. The aperture is typically a thin (opaque) metal sheet with openings that have well-known areas. The metal sheet will extend past the edge of a sample to make sure that no waveguiding occurs in the substrate. A standard, rigid aperture is preferable to a custom aperture from something like vinyl (e.g., electrical) tape, as such tapes can stretch and form curved edges. For small area devices (<1 cm²), an aperture is required for certified measurements. To establish if the designated area of a device is correct for an unapertured measurement, its current density can be compared to that of a measurement with an aperture. It is worth noting that in all cases, an aperture will necessarily lower the open-circuit voltage and alter the fill factor. Kiermasch et al. provide a mathematical framework of how this will affect device performance when temperature effects are ignored,[38] demonstrating that changes in voltage can be on the order of 100 mV. As historically current density has been the largest discrepancy between labs, apertures will remain necessary so long as the community measures small devices. However, changes in open-circuit voltage are often deeply tied to the science limiting device performance, whereas current is often more related to engineering optical transmission and absorption. This makes it worth measuring samples with and without apertures.

Current-Voltage Considerations: Hysteresis, Stable Power Output, Dynamic Current-Voltage

Finally, how to obtain the actual efficiency value of a PeSC has become a problematic issue since the first report of the strong hysteresis effect by Snaith et al.[18] For conventional solar cells, such as Si, CIGS, CdTe, the current-voltage (I-V) scan is commonly used to determine the PCE. However, the efficiency calculated from I-V scans for a perovskite solar cell could depend on the scan direction (i.e., reverse scan, where the bias is changed from open circuit to short circuit, or forward scan, where the bias is increased from short circuit to open circuit) and scan rate (i.e., how fast the bias voltage is changed during I-V scan). Figure S4A shows an example of the IV curves with both forward and reverse scans. The data were adapted from Kim et al.[39] In this example, the reverse scan yields a PCE of 19.7%, whereas the forward scan yields a PCE of 17.4%. The difference between these two PCEs with respect to one of these two PCE values (e.g., from reverse scan) is often used to describe the degree of hysteresis.[40] However, it should be noted that the degree of hysteresis can be strongly affected by the scan rates and thus should be used with care for comparison. Extensive efforts have been devoted to studying the underlying mechanisms contributing to the hysteresis, such as ion migration, charge extraction, ferroelectric behavior, capacitance, etc.[41–48] Impedance spectroscopy has become an effective method to study the impact of bulk and contact on the hysteresis behavior as well as the device stability in recent years.[49,50] Although this large hysteresis behavior of perovskite solar cells presents an unprecedented opportunity to study various interesting physical behaviors, it nevertheless presents a significant challenge for accurately determining the PCE based on the conventional IV scan. A recommended practice is to conduct the stable power output (SPO) near the maximum power point (MPP). An example of the SPO measurement is shown in Figure S4B for the same device shown in Figure S4A. This is normally done by biasing the device near the maximum power voltage and monitoring the current density output to stabilize, which can then be converted to the power output or the conversion efficiency. Because this measurement normally lasts for a few minutes with stable power output, it is generally accepted as a reliable way to verify or determine the PCE for devices with hysteresis. It is worth noting that a single measurement of SPO does not necessarily yield the maximum power output since the bias voltage is pre-determined or estimated using an IV scan. A more rigorous way is to conduct a series of SPOs over a range of bias voltages that will likely cover the MPP; the maximum PCE of this device will be determined by analyzing the voltage dependent SPOs.[51] This approach is similar to another method often called a dynamic, or asymptotic, IV. In the dynamic IV measurement, the device is scanned across the entire voltage range as in the conventional IV measurement with the device being held at each voltage step long enough to obtain the stabilized current output.[52] This asymptotic method has been adopted by accredited cell calibration labs such as NREL and Newport. A key criterion for this method is that the measured current is determined to be unchanging at the 0.05%–0.1% level. The measurement of SPOs or dynamic IV often takes a much longer time (e.g., minutes to tens of minutes) than that for the conventional IV measurement (e.g., seconds). Thus, the stability of the devices under the efficiency testing conditions becomes important and could be a significant challenge for certain types of devices. It is important to note that stable power output measurements should not be confused with measurements of long-term stability, which are beyond the scope of this paper. Measurements of long-term stability can be influenced by a variety of factors including load conditions (e.g., open circuit, short circuit, maximum power point), nominal operating cell temperature, ambient, frequency of measurement, and other measurement conditions. Typically, for these sorts of experiments, solar simulator requirements are relaxed due to the cost of
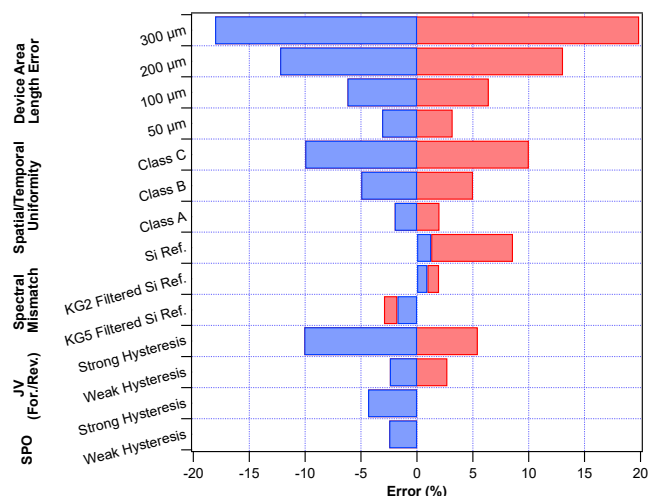
Figure 3. Tornado Plot of Standard Errors in PV Cell Efficiency Measurement
The device length error assumes a device area of 0.1 cm^2 with sides of actual length 3.16 mm. Each side is assumed to be longer or shorter by the length shown on the y axis. Spatial/temporal uniformity applies the maximum definition of spatial and temporal errors for different class simulators. Spectral mismatch error compares a MAPbI$_3$ cell to representative spectra from a new and older class A spectrum xenon lamp to different reference cells. The JV (For./Rev.) illustrates efficiency errors as measured relative to the asymptotic method for a device with strong hysteresis and one with weak hysteresis for various scan rates in the forward and reverse conditions. The stable power output (SPO) method illustrates efficiency errors for the same devices measured 20 mV off the Vmpp. Devices measured via the SPO method at V_{mpp} yielded the same value as the asymptotic method.

maintaining high spectral quality uniform light sources. Actual stability, with respect to light soaking on the scale of hours or more and shelf life for the scale of weeks, while desired by certification labs, is not required for record efficiencies at present. It is required, however, for the technology to advance.

Qualification and safety standards exist for commercial photovoltaic (PV) technologies (IEC 61215, 61730), with technology-specific variants for 61215. At present, there are no perovskite-specific standards, although there is an IEC working group (IEC TC82 WG2) that is actively discussing this. The perovskite community has largely followed the International Summit on Organic and Hybrid PV Stability (ISOS) consensus protocols as a framework to both age and report stability results,[36] which has a three-tier system for each aging type (e.g., ambient shelf life, heat, and damp heat for the different levels of dark storage). A recent update expands this framework beyond dark storage, light soak, outdoor, and thermal cycling to include light cycling and voltage bias tests, as well as formalizes an inert ambient variant for each type of test. The ISOS tests minimize the number of suggested conditions (e.g., ambient, 65°C, or 85°C) to facilitate comparisons between labs while providing varying levels of severity.[53]

Photovoltaic Error Comparison
The text above details many well-understood aspects of photovoltaic efficiency characterization that should be considered by the careful practitioner. To graphically compare the relative magnitude of these errors, a tornado plot was prepared for Figure 3. Some portions have definitional maximum errors such as the spatial and temporal errors associated with different class simulators. It should be understood that these particular errors are worst case scenarios, and methods potentially exist to

reduce the errors as described above, such as introducing an *in situ* monitor diode to renormalize for temporal fluctuations.

The other errors, however, required choosing specific cases, so should be understood as illustrative, not absolute. Area errors can be quite large for small devices, which are generally being used in the perovskite community. Using the incorrect area for a 0.1 cm² device can easily become the largest source of error, which helps explain the community's insistence on apertures when measuring small devices. The effect of spectral mismatch on even a class A spectrum can also be quite large and lead to overstating efficiency when using an improperly matched reference (here, for a MAPbI₃ cell). For the efficiency measurement approaches, the asymptotic scan method, which is used by NREL's certification group, is used as the zero-error case. Forward and reverse current-voltage scans are shown to be a plausibly large source of error depending on the level of hysteresis displayed by the device and scan conditions. It was found for both devices that the stable power output method agreed with the asymptotic method for the maximum power, but being off by as little as 20 mV could lead to sizable underestimation of the efficiency. The details of the measurements and device data are available in Figure S5 and Tables S2 and S3.

CHARACTERIZATION OF ORGANIC AND PEROVSKITE LIGHT-EMITTING DIODES

Definition of Key Radiometric and Photometric Parameters and Their Relationship

In evaluating the performance of any light source, it is important to understand the difference between radiometric and photopic quantities. Radiometric quantities are the actual physical quantities related to the energy carried by light. In contrast, a photometric quantity X_L corresponding to a given radiometric quantity X_R is obtained by weighting the spectral density of X_R at the wavelength of λ [= $X_R(\lambda)$] with the photopic response function $V(\lambda)$; i.e., the daylight human eye sensitivity as follows:

$$X_L = K_V \int X_R(\lambda) V(\lambda) d\lambda = K_V X_R^{(tot)} \int \rho(\lambda) V(\lambda) d\lambda \equiv K_V X_R^{(tot)} \gamma_V \qquad \text{(Equation 3)}$$

where K_V is the conversion factor given as 683 lm/W, $\rho(\lambda)$ is the spectrum of the light source normalized such that $\int \rho(\lambda) d\lambda = 1$ and $\gamma_V \equiv \int \rho(\lambda) V(\lambda) d\lambda$; i.e., the overlap integral between $V(\lambda)$ and $\rho(\lambda)$. Note that, in this formalism, $X_R(\lambda) = X_R^{(tot)} \rho(\lambda)$, where $X_R^{(tot)} \equiv \int X_R(\lambda) d\lambda$. The introduction of the normalized spectrum $\rho(\lambda)$ can be useful because spectral measurement can be done on a relative scale, not absolute.
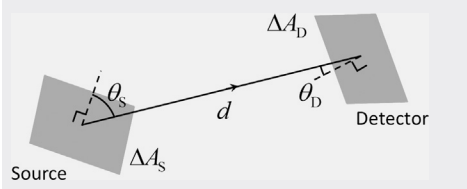
Radiometric quantities include radiant power, radiant intensity, irradiance, and radiance, and their corresponding photopic quantities are luminous power, luminous intensity, illuminance, and luminance (see Table 1 for definition and units of the radiometric and photometric terms and their use in radiant power transfer relation between a source and a detector).

The photometric conversion given by Equation 3 stems from the definition of the unit "candela" (cd)—one of the seven basic SI units—wherein 1 cd is given as the luminous intensity of a source emitting, in a given direction, the monochromatic radiation of 1/683 W sr⁻¹ with the frequency of 540 THz.[54] Note that this optical frequency corresponds to λ of 555.017 nm where $V(\lambda)$ is peaked. By definition, cd is equivalent to lm sr⁻¹, and $V(\lambda)$ is normalized such that its peak value is given by the unity so that the values in the other wavelength are given in a relative scale with respect to the value at the peak wavelength. This explains the origin that the luminous efficacy

Table 1. Definitions of Key Radiometric Quantities and Their Photometric Counterparts

Radiometric Quantities (X_R)	Definition	Corresponding Photometric Quantities (X_L)
Radiant power (Φ_R) [W]	energy carried per unit time by light	luminous power (Φ_L) [lm]
Radiance (L_R) [$Wm^{-2}sr^{-1}$]	radiant power per unit solid angle per unit projected area	luminance (L) [lm m^{-2} sr^{-1} = cd m^{-2} = nit]
Radiant intensity[a] (I_R) [Wsr^{-1}]	radiant power per unit solid angle	luminous intensity (I_L) [lm sr^{-1} = cd]
Irradiance (E_R) [Wm^{-2}]	radiant power per unit area	illuminance (E_L) [lm m^{-2} = lux]

Radiant Power Transfer Relation[b]

$$\Delta\Phi_R^{S\rightarrow D} = L_R \Delta A_S \cos\theta_S \times \frac{\Delta A_D \cos\theta_D}{d^2}$$

$$= I_R \times \frac{\Delta A_D \cos\theta_D}{d^2} = E_R \Delta A_D$$

(Equation 4)[b]

[a]Note that the term "intensity" is often used in physics and optics as a term synonymous with irradiance. Users should therefore be careful and read it in the context.

[b]$\Delta\Phi_R^{S\rightarrow D}$ is the radiant power transferred from a source with an area of ΔA_S and the radiance of L_R to a detector with an area of ΔA_D. The distance between the source and the detector is given by d. θ_S and θ_D are the tilt angles of the source and the detector, respectively, defined with respect to the line connecting the centers of the source and the detector.

K_V is given by 683 lm W^{-1} and that the photometric conversion involves the overlap integral shown in Equation 3. It is also noteworthy that $V(\lambda)$ is the function established by Commission Internationale de l'Éclairage (CIE) and equals $\overline{y}(\lambda)$—a color matching function used in CIE 1931 color space.[55] The tabulated values for $V(\lambda)$ are provided in Table S4.

Electroluminescence Efficiency

The EL efficiency is a performance parameter of prime interest for any LEDs. It includes current efficiency (η_{CE} [cd A^{-1}]), EQE (η_{EQE} [%]), and power efficiency (η_{PE} [lm W^{-1}]) as defined in Table 2.[16] As PeLEDs are made in the form of a thin-film device like OLEDs, their EL efficiencies are determined only with the photons emitted into the upper hemisphere (i.e., photons emitted backward and sideways are not accounted for, as they do not contribute to the generation of light in forward direction).

We have conducted a thorough literature search to illustrate the evolution of η_{CE} and η_{EQE} of green PeLEDs (Figure 4A and Tables S5–S7). The EL efficiency of PeLEDs has dramatically improved by engineering of interfacial layers,[7,56–60] electrodes,[61,62] perovskite film morphologies,[63–71] stoichiometry of precursors,[63,72] dimensional control,[73] and additives.[63,74–80] Recently, perovskite dots with ligands have been developed to effectively confine excitons in perovskite nano-crystals,[81–92] and the η_{CE} and η_{EQE} for red emission were increased up to 11.6 cd A^{-1} and 21.3% (η_{EQE} estimated from an angle-dependent measurement), respectively.[13] The high EQEs >20% were also obtained for near-infrared (NIR) emission from quasi-2D and 3D perovskite emitters with a wide-gap polymer (η_{EQE} = 20.1%)[11] and for green emission from perovskites mixed with MABr additives (MA = CH_3NH_3) (η_{CE} = 78 cd A^{-1}, η_{EQE} = 20.3% [Lambertian assumption]).[12] However, it is noted that the reported η_{CE} to η_{EQE} ratios vary rather widely from ca. 3 to 5 even for a similar device structure with the same EL spectra (Figures 4B and 4C), calling for establishing the standard protocols for the characterization of these EL efficiencies.

Table 2. The Efficiency of Light-Emitting Diodes with the Current Density of J and the Bias of V

Efficiency [Unit]	Definition
Current efficiency (η_{CE}) [cd A^{-1}]	luminance (L) per current density (J) at the viewing angle θ
	$$\eta_{CE}(\theta) = \frac{L(J;\theta)}{J} \qquad \text{(Equation 5)}$$
External quantum efficiency (η_{EQE}) [%]	the ratio of the number of the photons emitted into the upper hemisphere to the number of injected charged carriers
	$$\eta_{EQE} = \frac{\int \Phi_R^{(\text{upper hemisphre})}(\lambda) \big/ (hc/\lambda) d\lambda}{JA_S/e} \qquad \text{(Equation 6)}^a$$
Power efficiency (η_{PE}) [lm W^{-1}]	luminous power emitted into the upper hemisphere ($\Phi_L^{(\text{upper hemisphere})}$) per given electrical power input
	$$\eta_{PE} = \frac{\Phi_L^{(\text{upper hemisphere})}}{JVA_S} \qquad \text{(Equation 7)}$$

^{a}"A_S" is the active area of the light source under test. e, h, c, and λ are electronic charge, Planck constant, the speed of light in free space, and the wavelength of light, respectively.

Characterizing Method for Electroluminescence Efficiency of Perovskite Light-Emitting Diodes

Overview

One can obtain full radiometric quantities for simultaneous estimation of η_{EQE}, η_{PE}, and η_{CE} by using a goniometric setup where a detector is placed on a precision rotating arm perpendicular to the device plane with the center of the light source coinciding with the rotation center. The goniometric measurement for this task uses (1) a calibrated photodiode and a spectrometer in sequence, or (2) a spectroradiometer, which is a spectrometer calibrated for the absolute optical power. (Figure 5A). Although there is a case where one should measure radiometric quantities as a function of both θ and φ in a spherical coordinate system,[93] the azimuthal symmetry is satisfied as long as devices under test do not contain structures like a grating, etc. Hence, the analysis shown here assumes the azimuthal symmetry unless noted otherwise so that it may be all right to measure the radiometric quantities as a function of θ only. In the forthcoming description, we will further restrict ourselves to the case where a calibrated photodiode and a spectrometer are used in sequence. However, the equations expressed with L_R can be used as is for the method based on a spectroradiometer.

Upon estimation of the optical power transfer [$\equiv \Delta A \Phi_R^{S \to D}(\theta)$] from a flat light source with the area of ΔA_S to a detector with the area of ΔA_D, it can be shown that $\eta_{CE}(\theta)$, η_{PE}, and η_{EQE} are given as Equations 8–10 in Table 3 (see Supplemental Information for the detailed deviations). That is, once one measures i_{ph} and $\rho(\lambda)$ as a function of the observation angle θ, $L_R(\theta)$ and all the important efficiencies can be identified with the equations shown above. Typically, the goniometric measurement procedure may be divided into three parts. The first part is to measure the photodiode current at the normal direction, changing the voltage or current applied to the light source so that one can obtain the J-V characteristics and determine the proper sourcing conditions for the subsequent measurement steps. The second part is to measure the photodiode current while varying the observation angle θ from 0° to near 90° under the fixed sourcing condition. The third part is to measure the relative spectrum while varying θ from 0° to near 90° under the same sourcing condition as the photodiode measurement. After
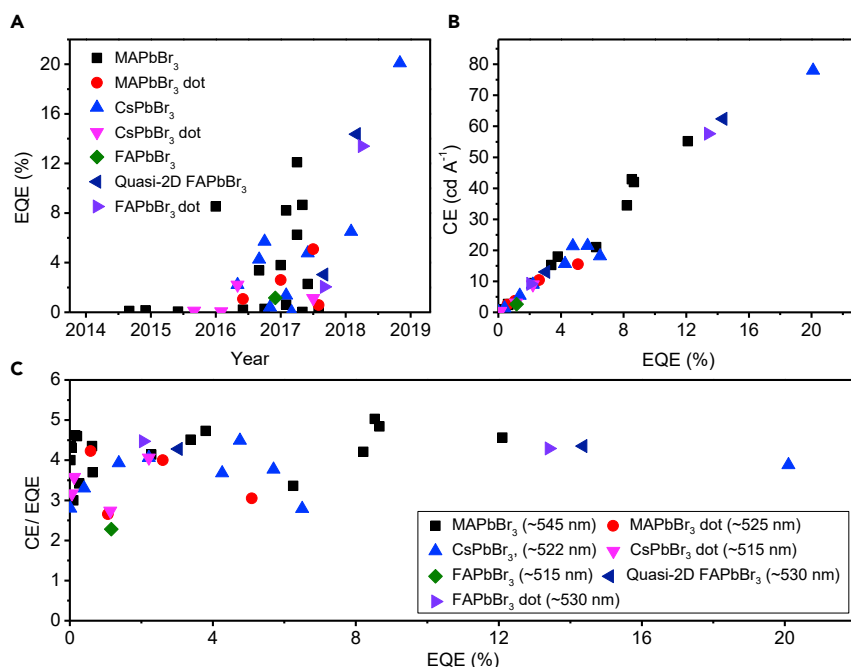
Figure 4. Progress in EL Efficiency of Perovskite LEDs
(A) External quantum efficiencies of the green-emitting perovskite LEDs versus year published.
(B) Current efficiency of the green-emitting perovskite LEDs versus their calculated external quantum efficiencies.
(C) Ratio of current efficiency to external quantum efficiency of green-emitting perovskite LEDs.

all measurements, $i_{ph}(\theta)$ and three integrals $\gamma_{PD}(\theta)$, $\gamma_V(\theta)$, and $\gamma_\lambda(\theta)$ in Equations 11, 12, and 13 can be identified for a given sourcing condition, so that one can estimate $L_R(\theta)$, $L(\theta)$, $\eta_{CE}(\theta)$, η_{EQE}, and η_{PE} with Equation 3 and Equations 8S–10S in Table 3. As an additional note, it is useful to use the numerical value of $\frac{hc}{e} \approx 1240$ W A^{-1} in Equation 9 if the unit of wavelength is given in nanometers.

While the goniometric measurement can be rather time consuming, the availability of a computer-controllable, motorized rotation stage and a source measurement unit with standard general purpose interface bus (GPIB) interfaces can make the overall measurement steps fully or semi-automatic. It is recommended that devices are housed in a sample holder that can provide a stable mechanical housing and secure electrical connection during the measurement. The overall setup is then placed in a black, light-tight enclosure equipped with a port for external electrical connections. Using typical compact fiber-optic spectrometers, the enclosure could be made small enough to be placed in an N$_2$-filled glove box to prevent degradation of devices by the surrounding environment during the measurement.

In the setup shown in Figure 5A, one may think the role of a photodiode and a fiber-optic spectrometer can be redundant because some fiber-optic spectrometers can be factory calibrated to function as spectroradiometers. Nevertheless, the size of the input port is typically much smaller than the photodiode, and thus it tends to require a longer integration time to obtain sufficient signals, which could be disadvantageous for PeLEDs, which are often subject to fast operation-induced degradation. Furthermore, the overall measurement accuracy is not compromised by a variation in light coupling into an optical fiber, as the fiber-optic spectrometer in the setup shown in Figure 5A is not used for absolute power measurement. In practice, the
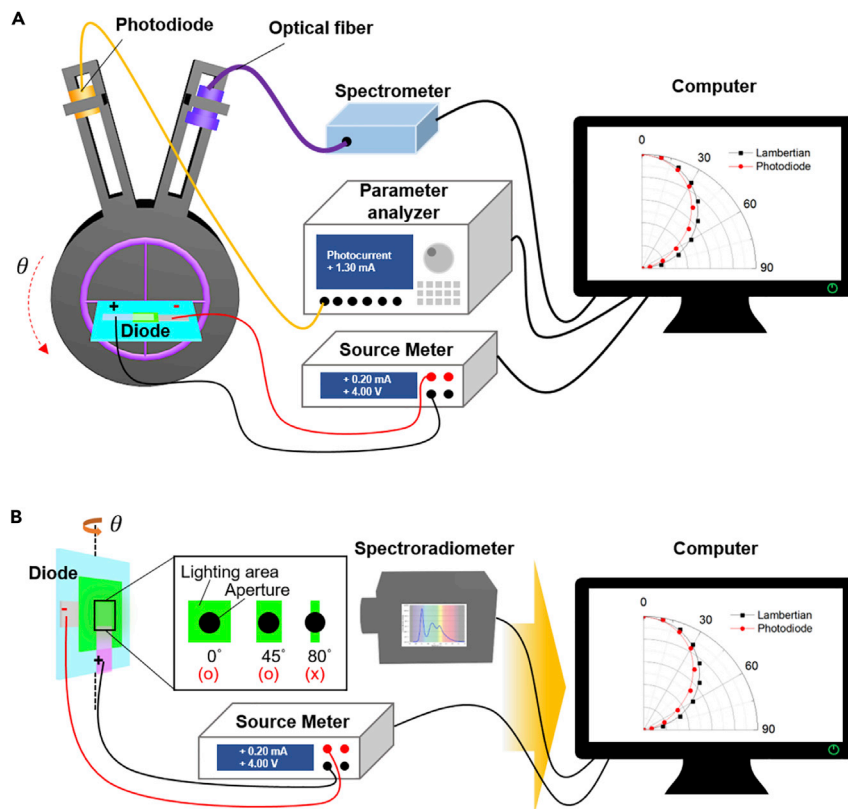
Figure 5. Schematics of EL Efficiency Characterizing Methods
(A) Goniometric measurement based on a calibrated photodiode and a fiber-optic spectrometer.
(B) Goniometric measurement based on a spectroradiometer.

angular intensity profile can quickly be measured with the calibrated photodiode at finer steps of angle, and the emission spectra may be separately measured at wider steps of angle, if the samples are severely subject to operation-induced degradation. The latter can be justified from the fact that the angular spectral shift is relatively small in PeLEDs because of its narrow emission spectrum. Details will be provided in the following sections.

The goniometric measurement can provide the most complete information on the emissive properties of light sources under test, and so it is highly recommended for research and development (R&D) stages, which may involve changes in materials or device structures. Furthermore, if combined with an index-matched half-ball or half-cylinder lens, this measurement can shed light on some of the internal modes as well, helping one to better grasp the full details of the optical properties of the light source under study.

Lambertian Approximation and Its Limitation
Some planar light sources exhibit the same radiance regardless of the viewing angle. That is, $L_R(\theta) = L_R(\theta = 0) \equiv L_{R0}$. Such a light source is called Lambertian source. If $\rho(\lambda)$ is independent of θ, then $L(\theta)$, $\gamma_{PD}(\theta)$, $\gamma_V(\theta)$, and $\gamma_\lambda(\theta)$ are also angle-independent. This greatly simplifies the integrals in Equations 9a and 10a and makes it possible to obtain η_{EQE} and η_{PE} directly from η_{CE} measured at $\theta = 0$, as shown in Equations 9b and 10b. Typical bottom-emitting OLEDs with little cavity resonance effect often exhibit Lambertian characteristics, and thus such

Table 3. The Equations in the Goniometric Measurement of Efficiencies

Efficiency [Unit]	Equations		
	General Case		Lambertian $(L_R(\theta) = L_R(0) = L_{R0}\,;\,L(\theta) = L(0) = L_0)$
η_{CE} [cd A^{-1}]	$\eta_{CE}(\theta) = \dfrac{K_V \gamma_V(\theta) L_R(\theta)}{J}$	(Equation 8a)	$\eta_{CE}(\theta) = \eta_{CE}(\theta = 0)$ (Equation 8b)
η_{EQE} [%]	$\eta_{EQE} = \dfrac{\pi}{J}\left(\dfrac{e}{hc}\right) \times 2\displaystyle\int_{\theta=0}^{\pi/2}\gamma_\lambda(\theta)L_R(\theta)\cos\theta\sin\theta\,d\theta$ (Equation 9a)		$\begin{aligned}\eta_{EQE} &= \dfrac{\pi}{J}\left(\dfrac{e}{hc}\right)\gamma_\lambda L_{R0}\\ &= \pi\left(\dfrac{e}{hc}\right)\dfrac{\gamma_\lambda}{K_V\gamma_V}\eta_{CE}\end{aligned}$ (Equation 9b)
η_{PE} [lm W^{-1}]	$\eta_{PE} = \dfrac{2\pi K_V}{JV} \times \displaystyle\int_{\theta=0}^{\pi/2}\gamma_V(\theta)L_R(\theta)\cos\theta\sin\theta\,d\theta$	(Equation 10a)	$\eta_{PE} = \dfrac{\pi K_V L_{R0}\gamma_V(\theta=0)}{JV} = \dfrac{\pi L_0}{JV} = \dfrac{\pi\eta_{CE}}{V}$ (Equation 10b)

Where:

$\gamma_{PD}(\theta) = \int R_{PD}(\lambda)\rho(\lambda,\theta)d\lambda$ (Equation 11)

$\gamma_V(\theta) = \int V(\lambda)\rho(\lambda,\theta)d\lambda$ (Equation 12)

$\gamma_\lambda(\theta) = \int \lambda\rho(\lambda,\theta)d\lambda$ (Equation 13)

$L_R(\theta) = \dfrac{L(\theta)}{K_V\gamma_V(\theta)} = \dfrac{i_{ph}(\theta)}{\gamma_{PD}}\dfrac{d^2}{\Delta A_S \Delta A_D \cos\theta}$ (Equation 14)

$\rho(\lambda)$, $V(\lambda)$, K_V, i_{ph}, and $R_{PD}(\lambda)$ are the emission spectrum of a light source normalized so that the area under the curve becomes the unity, viewing angle, photopic response curve, photopic conversion factor of 683 lm/W, the photocurrent of a photodiode, and the spectral responsivity of a photodiode, respectively. The other terms in Equation 14 are defined in Table 1.

simplification has been accepted to some degree in the OLED research field. However, even with the bottom-emission configuration, for example, cavity resonance can become non-negligible depending on the thickness of a transparent conductive oxide layer,[94,95] leading to non-Lambertian characteristics. Cavity resonance effect can become significant even in bottom-emitting configurations if the total optical thickness; i.e., the summation of the refractive index times the physical thickness for each layer including ITO, organic or perovskite layers, and oxide buffer layers, equals $3/4\lambda$ or $5/4\lambda$. In such a case, the normalized angular intensity profile can depart easily from that of a Lambertian light source because resonance condition is met only at a normal direction. Angular characteristics can also be affected by the location of the emission zone; so one should always be careful about the validity check of Lambertian approximation. Presence of internal nano- or micro-structuring, if any, can also lead to non-Lambertian emission characteristics.[95] As will be discussed later, the narrow spectral emission of PeLEDs makes them more prone to formation of non-Lambertian characteristics than typical OLEDs. That is, extreme care has to be taken not to overuse the Lambertian simplification as there are many cases where Lambertian approximation fails.

Further Note on the Goniometric Measurement with a Spectroradiometer

As noted earlier, a goniometric measurement can be realized with a spectroradiometer. In this case, a light source under test is often rotated while the spectroradiometer is fixed due to its relatively large size (Figure 5B). The spectroradiometer commonly used in the field is equipped with an imaging optics so that it measures the spectral radiance of the emitted light from an aperture part of a given light source. This is useful, for example, when measuring radiometric quantities from a particular pixel in a display panel. Due to its bulky nature, measurement involving the spectroradiometer is usually conducted in an ambient atmosphere; in such a case, devices should be encapsulated in an inert atmosphere to prevent them from getting degraded by the surrounding environment during the measurement.
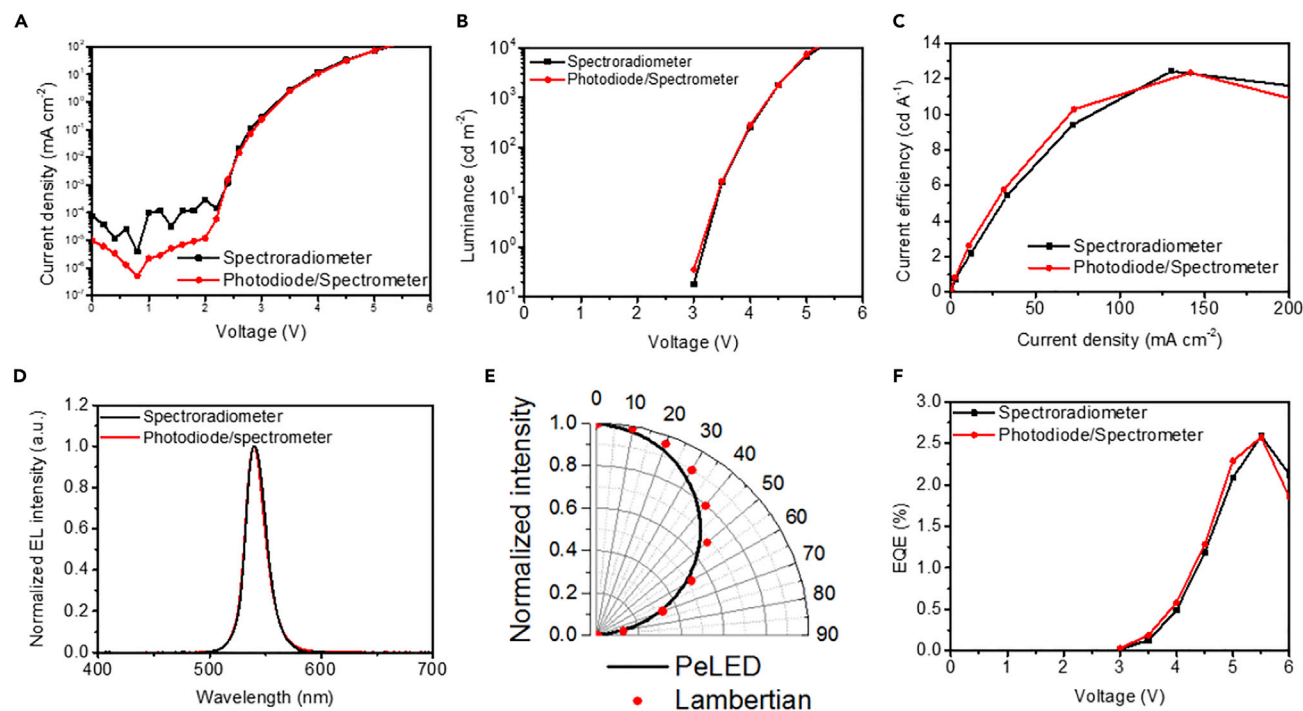
Figure 6. Comparison of EL Characteristics of PeLEDs Obtained from Photodiode and Spectrometer-Based, and Spectroradiometer-Based, Goniometric Measurement Systems
(A) Current density.
(B) Luminance.
(C) Current efficiency.
(D) EL spectrum.
(E) Viewing angle-dependent emission profile.
(F) EQE.

Figure 6 is the comparison of EL characteristics of PeLEDs measured by the photodiode and spectrometer- or spectroradiometer-based goniometric systems. We used the previously reported PeLED structure: ITO/self-organized conducting polymer (50 nm)/MAPbBr$_3$ (400 nm)/2,2',2''-(1,3,5-Benzinetriyl)-tris(1-phenyl-1-H-benzimidazole) (TPBi) (50 nm)/LiF (1 nm)/Al (100 nm).[63] The experimental details are included in the Supplemental Information. Regardless of the measurement tools, similar results were obtained. It was confirmed that both methods yielded similar results. The slight difference in each curve came from the pixel-to-pixel deviation of PeLEDs. This comparison experiment well-illustrates that a relatively inexpensive setup based on a calibrated photodiode and a spectrometer can be used to obtain an accurate result as long as the angular variations in the intensity and emission spectra are correctly taken into account as described above.

Measurement Using an Integrating Sphere
An integrating sphere system can also be used to characterize η_{EQE} and η_{PE} of OLEDs and PeLEDs.[16,82,96–100] The system is typically combined with a non-imaging spectroradiometer and measures total radiant power, Φ_R. Due to the spectrally neutral, highly diffusive inner wall of the integrating sphere, it can gather all photons emitted toward upper hemisphere, and therefore, viewing angle-dependent emission profiles are not required to calculate η_{EQE}. To obtain an accurate η_{EQE}, the light emitted from the substrate edges following in-plane waveguiding must be excluded. For instance, it can be done by applying thick black

paint along the edges of a device or by surrounding them with a black tape. Alternatively, the device may be placed right outside the input port of the integrating sphere so that only the forward output can be coupled into the integrating sphere, as previously reported by Dai et al.[99] and Wang et al.[100] In addition, a baffle is placed inside the integrating sphere to prevent the emitted light from reaching the exit port directly (Figure S8).[98] Therefore, the geometry inside the integrating sphere must be carefully controlled to avoid an erroneous η_{EQE}. The method using an integrating sphere is convenient as it does not require time-consuming angle-dependent measurement. However, the integrating sphere system does not provide angle-resolved data. Therefore, a separate system for measuring angle-resolved EL must be accompanied if one wants to obtain η_{CE} as a function of the observation angle.

Avoiding Measurement Discrepancy and Errors
Errors Due to Lambertian Approximation

In the previous section, we noted Lambertian approximation as a source of potential errors in characterization of η_{PE} and η_{EQE}. This limitation can be even more severe when it comes to PeLEDs. Presence of cavity resonance and/or the relative location of electric field maxima with respect to the location of an emitting zone can lead to non-Lambertian angular characteristics. The former is because the peak resonance is blue shifted when observation angle (θ_{ob}) increases, and thus the spectral overlap of the emitter photoluminescence (PL) spectrum with Fabry-Perot resonant curve varies depending on θ_{ob}.[101] It is apparent that the emitter with a narrow PL spectrum will go through rapid change in the spectral overlap (and thus the intensity) as θ_{ob} changes. In addition, it is also known that the location of the emission zone can influence the angular intensity profile significantly, as demonstrated by Fries et al.[102]

While the discussion made above holds for both OLEDs and PeLEDs, the narrow-band emission of perovskite emitters makes PeLEDs subject to formation of more severe non-Lambertian angle dependence of intensity than those of OLEDs.[17,18] This is because the angle-dependent mismatches to the normalized Lambertian intensity profile ($\sim\cos\theta_{ob}$) mentioned above can have a more significant effect when the PL emission is narrow than when it is broad. The example shown in Figure 7A well-illustrates that thin-film LEDs with the PL FWHM of 20 nm—typical of MAPbBr$_3$-based PeLEDs—can indeed show, in some geometry, the emission characteristics that are quite far from the Lambertian characteristics, while those with the PL FWHM of 100 nm exhibit relatively mild deviations from the Lambertian characteristics in the same geometry. For example, in the device configuration where glass/ITO (150 nm)/hole transport layer (HTL) (30 nm)/ emission layer (EML) (70 nm)/electron transport layer (ETL) (d_{ETL})/Al(100 nm), with d_{ETL} being 0, 50, and 70 nm, the case with d_{ETL} = 70 nm is shown to yield a strong contrast in the angular intensity profiles between emitters with FWHM values of 20 and 100 nm. The physical origin is well illustrated in Figure 7B by the different trend in the spectral overlap between PL and the Fabry-Perot resonance envelop curve versus observation angle. For this reason, Lambertian approximation would rather be avoided in PeLEDs, and full goniometric measurement is highly recommended for the accurate estimation of η_{EQE} and η_{PE} of PeLEDs. Please refer to Figure S9 for the experimental data showing sub- or super-Lambertian characteristics of PeLEDs and Table S8 for estimation of the error in EQE that can be caused by the improper Lambertian approximation for these non-Lambertian PeLEDs.
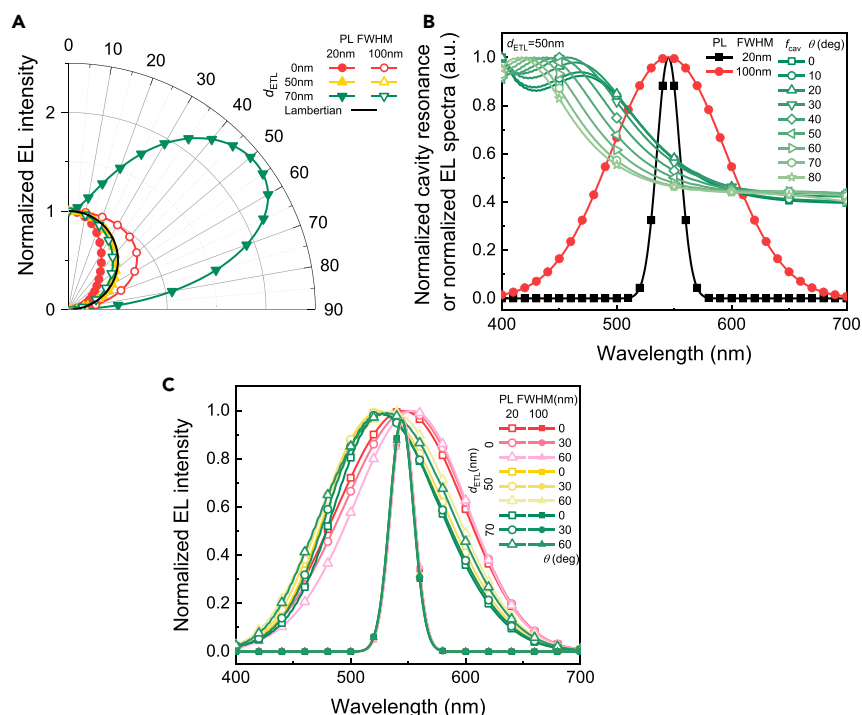
Figure 7. Simulated Angle-Dependent EL Characteristics of MAPbBr₃ PeLEDs with FWHM of 20 and 100 nm

(A) Viewing-angle (θ)-dependent normalized intensity profile of EL versus the ETL thickness. PeLED structures used in the simulation were glass/ITO (150nm)/HTL (30nm)/EML (70nm)/ETL (d_{ETL})/Al(100nm) with d_{ETL} being 0, 50, and 70 nm, where HTL and EML refer to hole transport layer and emissive layer, respectively. The black solid line indicates that of a Lambertian light source (i.e., cosθ). It is noted that departure from ideal Lambertian characteristics can be severe for some d_{ETL}s when FWHM is small.

(B) The angle-dependent spectral overlap between Fabry-Perot cavity resonance curve and PL emission spectra: comparison at d_{ETL} = 70 nm between emitters with PL spectra having FWHM of 20nm and 100nm.

(C) EL spectra versus viewing angles of 0°, 30°, and 60° for d_{ETL} of 0, 50, and 70 nm. Comparison is made for those with emitters having FWHM of 20 and 100 nm. It is noted that the angle-dependent spectral shift becomes fairly small for devices with narrower FWHM than for those with wider FWHM.

For modeling, we assumed lossless EML, isotropic emitter orientation, and Gaussian distribution of PL spectrum with the 20 or 100 nm FWHM. Emission was assumed to be at the EML/HTL interface. Refractive indices of HTL, EML, and ETL used in the simulation were set as 1.75, 2,47, and 1.75, respectively. Calculation was done with the transfer-matrix formalism for a dipole embedded in a planar microcavity, which takes into account the Purcell effect.[102]

Spectral Error

The EL spectrum of PeLEDs is distributed typically over a far narrower spectral range than that of OLEDs. In the PeLED presented in Figure 8, the FWHM value of the measured PeLED EL spectrum is as small as 21.5 nm, while that of a green OLED with Ir(ppy)₃ emitter has ca.70.5 nm (Figure 8A). This narrow spectral emission of PeLEDs is generally regarded as highly beneficial for wide color gamut when used as primary colors in a display; however, it tends to make PeLEDs subject to a relatively large error in η_{CE} if there is a spectral error. For the devices presented in Figure 8, the relative errors of up to ca. −6.3% and −16.6% are expected for η_{CE} in the case of MAPbBr₃-based PeLEDs when the overall emission spectrum is shifted by 10 and 20 nm, respectively. (Figure 8B) This is in contrast with the case of Ir(ppy)₃-based OLEDs that show up to 3.5% and 9.1% errors for the same spectral shift of 10 and 20 nm, respectively.
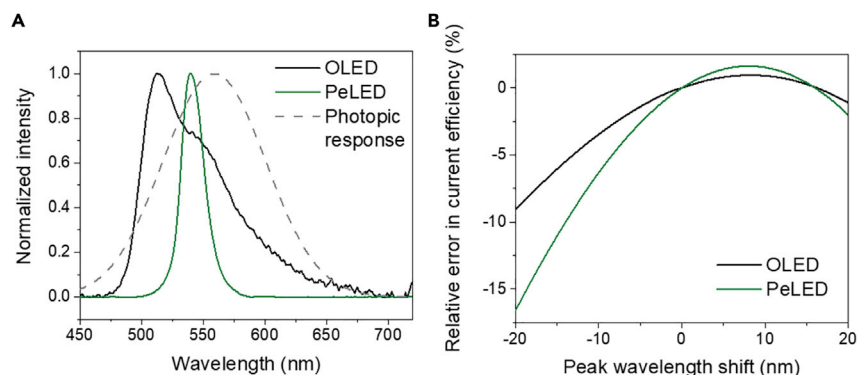
Figure 8. Simulated EL Efficiency Change Depending on Peak Shift of EL Spectrum
(A) The EL spectrum of OLED with Ir(ppy)$_3$ emitter and PeLED with MAPbBr$_3$. Dashed line indicates human photopic response function.
(B) Relative error in the current efficiency of OLED and PeLED expected for a given peak shift in their EL spectra.

In practice, spectral error may originate from a poor spectral calibration of a spectrometer. Calibration of a spectrometer is usually done by recording the response of its sensor to a reference light source, the spectrum of which is already known. For example, in-house calibration can be done at low cost by adopting a tungsten-halogen lamp as a reference source equivalent to a black body held at 3,000 K. This could be all right for green to NIR region, but it could be problematic in blue and UV range because the tungsten-halogen lamp has little spectral power density in that spectral region. Therefore, it is highly recommended that a spectrometer is factory calibrated on a regular basis, with a reference light source having a wide range of spectral output that covers the whole spectral range of concern. Combination of a deuterium light source and a tungsten-halogen light source can be a good candidate for a reference light source covering from UV to NIR.

Luminescence Efficiency Error Comparison
The relative errors in η_{EQE} and η_{CE} versus their various causes are presented in Figure 9. In this calculation, it was assumed that the device has the active area of 2 × 2 mm^2 and that detectors are held by rotating arms in the goniometric characterization system as shown in Figure 5. For η_{CE}, it was assumed that measurement is done for a direction normal to the device substrate.

As PeLEDs or OLEDs made in labs are often quite small, i.e., typically less than 1 cm^2, an incorrect measure of the device length can be the largest source of errors. The misalignment of shadow mask in the evaporation process of electrodes can cause this type of error. If one side of the device length is overestimated by 0.3 mm (15%), the resulting efficiency is lowered by 13%. This type of error is universal because all the optical calculations are based on the device area. The intensity deviation at the off-axis angle can be another major source of error for η_{EQE} estimation. Note that the detected optical power is a projected value and the error is amplified in the inversion process to calculate the original value. In order to illustrate the significance of this source of error in a quantitative manner, note first that $I(\theta)/I(0) = \cos^n\theta$ can conveniently be used as a model formula for the normalized angular intensity profile of a given light source for super-Lambertian ($n < 1$) or sub-Lambertian ($n < 1$) characteristics. This is because $\cos^n\theta$ with $n < 1$ ($n > 1$) is always larger (smaller) than $\cos\theta$; i.e., the normalized angular intensity profile of a Lambertian light source, as $0 < \cos\theta < 1$ for $0 < \theta < \pi/2$. When the normalized angular intensity profile $I(\theta)/I(0)$ is mistakenly measured to follow $\cos^n\theta$ with $n \neq 1$ for a light source that is actually
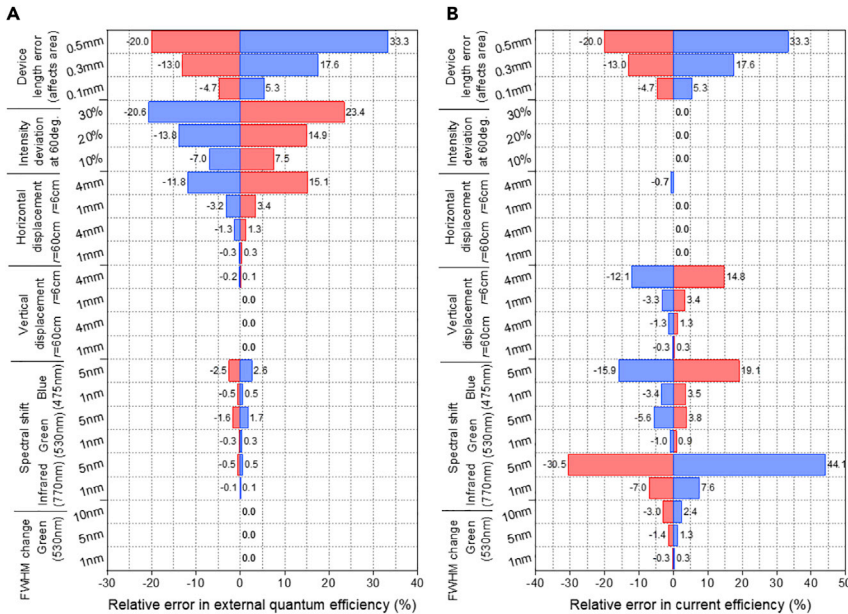
Figure 9. Tornado Plot of Potential Errors in Estimation of η_{EQE} (left) and η_{CE} (right) of a PeLED Device with the Square Device Area of 4 mm² in the Goniometric Setup Shown in Figure 5

Lambertian ($n = 1$), for example, even a slight departure can lead to a significant error in η_{EQE}. For example, mistakenly measured super-Lambertian profile modeled with $n = 0.86$, which yields 10% overestimation of the intensity at 60 degrees with respect to Lambertian profile ($n = 1$), leads to overestimation of η_{EQE} by 7.5%. (Refer to Figure S10 for further details.)

In a detector-rotating goniometric measurement, the light source must be located at the center of rotation. If the position is off center, there will be a change of distance between the sources and detector during the angular sweep. Moreover, the polar angle will be different from the intended value. Note that the horizontal displacement breaks a symmetry in angular intensity profile. In a device with axial symmetry, it is thus easy to detect this type of error by measuring at both positive and negative angles and comparing their mirror symmetry. It is noteworthy that the magnitude of error gets larger when the source-to-detector distance (r) becomes smaller. The calculation in Figure 9 was done for $r = 6$ cm and $r = 60$ cm, respectively, for the sake of comparison (further details on calculation are found in Figures S11 and S12). If the source was horizontally displaced by -4 mm, the estimated EQE will have a relative error as large as -11.8% for $r = 6$ cm when the angular profile at positive angles was used. Therefore, it is important to ensure a source-to-detector distance to be large enough within the dimensional constraints set by the lab environment. However, the optical power coupled to a detector scales with $1/r^2$, and thus one may need to set a long integration time for detection if r is too large. In such a case, the time that it takes for each measurement could become very long unless a device is driven at a higher brightness. Both can be critical for PeLEDs with a limited operation lifetime. Therefore, an optimal source-to-detector distance should be chosen considering the immunity to the geometrical error and the measurement duration for the full angular sweep.

Even with -1 mm horizontal displacement, which is only 1/60 to the source-detector distance for $r = 6$ cm, η_{EQE} can have more than 3% relative error due to the

accumulation of errors in all the angles. For η_{CE} defined at normal direction, however, the error contributed by this horizontal displacement error is relatively small and often negligible unless r is too small.

The vertical displacement of a light source or detector can happen when a source or detector is displaced from the intended height due to loose fixtures, etc. It does not break the angular symmetry of measurement, and thus it is hard to detect this type of error. Since the intensity recorded with a detector with a given device area is proportional to $1/r^2$ rather than $1/r$, the error can be rather significant. This type of error can even cause the angular intensity of Lambertian emitter to look like a non-Lambertian angular profile, as presented in Figure S13. For example, if the vertical displacement overestimated the intensity at near normal direction, then the intensity measured at a higher angle could be underestimated. In such a case, compensation can make overall η_{EQE} have almost no error, but not for η_{CE}, which is directly affected by the intensity change in the normal direction. Regardless of the errors in these efficiencies, one should ensure the vertical displacement is kept as small as possible for a correct account of the angular emission profile.

Although it is not usual to have a distorted spectrum, it could also happen when the spectrometer calibration is off for any reason. Since typical PeLEDs have a narrow EL spectrum, in particular, the wavelength calibration becomes important. If the center wavelength is shifted due to the crude calibration, η_{CE} can be subject to a relatively large error because the spectral overlap between the EL spectra and the photopic response significantly affects the candela value of the light source. The spectral overlap between the EL spectra and the photodiode response curve is also a factor that can influence the accuracy of η_{CE} via spectral miscalibration. Note that estimation of EQE also involves spectral overlap integrals that include EL spectra, and thus EQE could also be subject to similar errors. The effect on EQE, however, is rather small because the integrands in the spectral integrations of interest have similar functionality over λ and those integrations appear on both the nominator and denominator, almost cancelling the effect of each other (further information on calculation is found in Figures S14 and S15 and equations therein). It is also noted that this spectral-shift-induced error can depend on the spectral range of a light source. For example, a 1-nm shift of the center wavelength makes 1% error in η_{CE} for green PeLEDs, but more than 7% error for an NIR device.

To sum up, η_{EQE} has a relatively high sensitivity on the angular intensity error and the horizontal displacement of the sample position. For the current efficiency, it is subject to errors, especially for vertical displacement of the sample position, as well as for the spectral miscalibration.

Errors Due to the Operational Instability of PeLEDs

In spite of many researchers' efforts, the operation lifetime of PeLEDs is often limited due to the intrinsic instability of MHP materials.[103] During a scanning measurement for characterizing PeLEDs, their EL properties as a function of current density can be degraded. If a PeLED under test indeed has a low operation stability, the degradation during a scanning measurement of angle-dependent EL emission can severely distort the profile, resulting in an erroneous η_{EQE}. One way to figure out whether a goniometric measurement is valid and free from such distortion is to scan the angle-dependent EL from $-90°$ to $+90°$ and to check if the bilateral symmetry with respect to the viewing angle of $0°$ can be met (Figure S16).

In a case where the operational stability is still of an issue, it could be wise to measure the angle-dependent EL at wider steps (e.g., at a step of $10°$) and use an
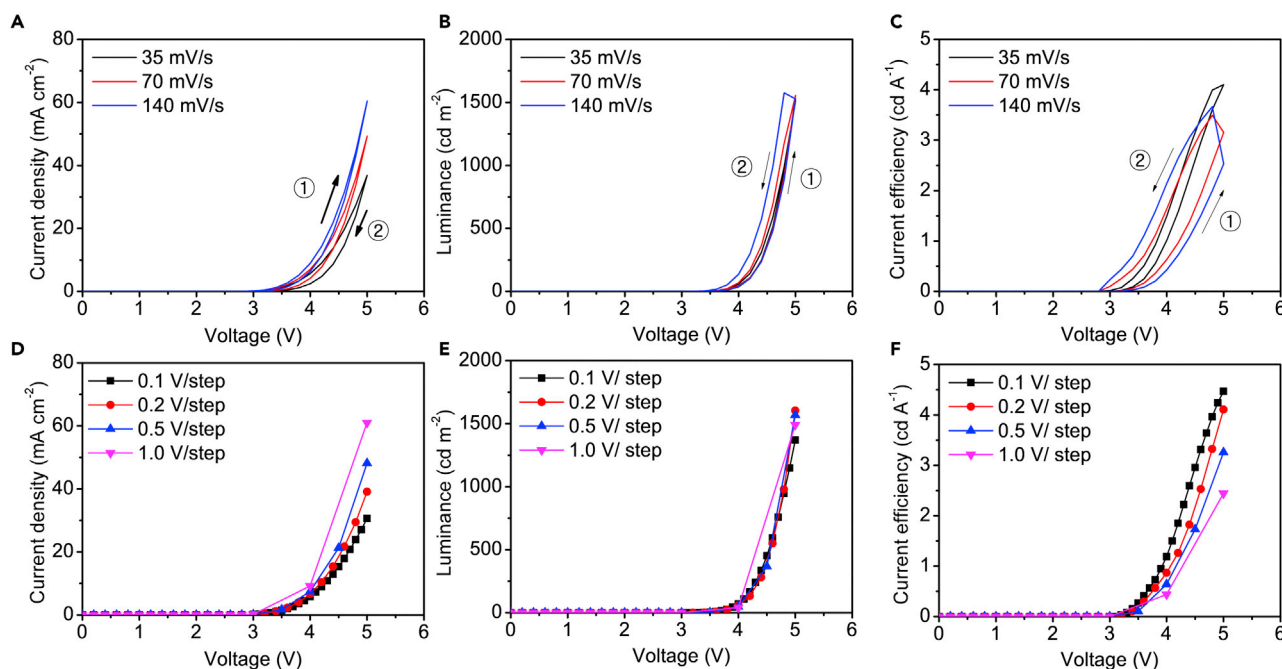
Figure 10. Scanning Rate, Direction, and Step-Size-Dependent EL Characteristics of PeLEDs
(A–C) Hysteresis analysis of *J-V-L* characteristics of PeLEDs. (A) Current density, (B) luminance, and (C) current efficiency.
(D–F) *J-V-L* characteristics of PeLEDs depending on scanning step size. (D) Current density, (E) luminance, and (F) current efficiency.

interpolation scheme so that the device operation time can be kept minimal. In such a case, authors should describe the detailed procedure in the experimental sections and, if possible, provide a typical error coming from such simplification. Furthermore, one would rather drive the device at current density (*J*) that is not too high, provided that a sufficient level of signal-to-noise ratio (SNR) can be secured during the spectral measurement.

Scanning Rate and Direction-Dependent EL Properties
Scanning rate and direction during measurement have been reported to strongly affect the EL efficiency of PeLEDs, unlike OLEDs (Figure 10).[17] Ionic characteristics of MHP allows ionic motion under the electrical bias condition, and redistribution of ionic species in MHP that fills trap states and reduces interstitial defects can improve PL and EL characteristics of PeLEDs.[104] However, when a high electric field (or long-term electrical stress) is applied to PeLEDs, external bias begins to break original perovskite lattice and leads to generation of more defects that induce non-radiative recombination, which can be attributed to "non-excess" ion migrations by high (or long-term) external field. The scanning rate and direction affect EL characteristics of PeLEDs (Figures 10A–10C). The lower scanning rate (i.e., longer biasing time) resulted in more *J-V* hysteresis on forward and backward direction scanning of PeLEDs (Figure 10A); the result seems to be influenced by ion migrations and material degradation under longer timescale electrical biasing in the low scanning rate measurement. However, the higher scanning rate measurement showed larger hysteresis of luminance characteristics, and the luminance was higher at a given voltage during backward direction scanning in all measurement conditions (Figure 10B). The higher rate measurement makes a larger increase in luminance during backward direction scanning, which could be attributed to the trapped-charge-assisted recombination within the perovskite layer, rather than the injected charge carriers by an external bias. As a result, the current efficiency

increases during the backward direction, even though the forward bias condition renders higher current density (Figure 10C). The scanning direction and rate dependency of PeLEDs could be attributed to ionic motion under the external electric field in the perovskite materials and also the trapped charge carriers under given scanning rate and direction. Furthermore, Kim et al. have recently showed that the maximum achievable efficiency of PeLEDs can be influenced by pulsed driving as opposed to conventional DC driving.[105] Using a relatively wide voltage step during the J-V-L scan can also be helpful in relieving the degradation-related issue (Figures 10D–10F). However, when one adopts this wide step (e.g., 0.5V– 1V) for *J-V-L* measurements, it can introduce errors in pinpointing the condition and value for the maximum EL efficiency although it provides the correct EL efficiency at each specific measured point of *J*, *V*, and *L*. Future researches for PeLEDs must consider the scanning rate and direction-dependent EL characteristics and be conducted to reduce the dependency for the commercialization of PeLEDs.

DISCUSSION

As the efficiency of perovskite optoelectronic devices including PeSCs and PeLEDs has been dramatically increased in recent few years, accurate characterization of the efficiency has become a very important issue for the reliability of research on PeSCs and PeLEDs. Unlike the case of conventional organic optoelectronic devices, factors such as hysteresis and dependence on scanning direction and rate must be taken into account with great care. The PeSCs with record PCEs are now strictly certified by the international certification labs; for instance, the National Renewable Energy Laboratory (NREL) and the Newport Corporation in the United States, the National Institute of Advanced Industrial Science and Technology (AIST) in Japan, and the Fraunhofer Institute for Solar Energy (ISE) Laboratory in Germany. This perspective is partially an attempt to help reduce surprises when cells get certified and improve the overall quality of reported data. A "PV reporting checklist" has been included as a supplement with both general considerations and an actual checklist.

While the certification authority for record efficiency of PeLEDs does not exist, our guidelines would improve the reliability in the uprising research on PeLEDs. This would help researchers in fields develop the best measurement practice and find proper ways to realize the maximum efficiency that PeLED technologies can eventually offer. To provide quick insight on the maximum achievable EQE of bottom-emission PeLEDs, we calculated optical mode fractions of ideal PeLEDs with four representative refractive indices of EML (Figure S17). According to the simulation result, maximum achievable EQE is higher than 30% for bulk perovskite film-based PeLEDs and 24% for low-dimensional perovskite nanocrystal-based PeLEDs. Beyond efficiency, device lifetime, especially operation lifetime, also must be taken into account when characterizing the devices. Accurate measurements to reduce an erroneous efficiency will boost the research on perovskite optoelectronics, giving reliable and consistent research results. Finally, unclear understanding of the mechanism on the poor stability of perovskite-based devices has become one of the most critical hurdles to further development toward commercialization. Over the past several years, we have witnessed, for PeSCs, significant progress on stability studies ranging from basic materials issues to device and module level operation. However, one of the main issues currently facing this field is the inconsistences in reporting experimental details and stability test conditions. Perovskite materials and device operation can be affected by many factors such as the ambient temperature, humidity, oxygen, pressure, spectrum, and intensity of light illumination, and bias voltage of devices. It is even more complicated, as many of these factors often do not have a

simple impact on the stability and new mechanisms that often arise when two or more factors are combined. Thus, it is important for researchers to follow standardized test conditions as much as possible and also clearly report the test conditions when drawing a conclusion. This practice will enable more meaningful interlaboratory comparisons. The organic photovoltaics community addressed these same issues a number of years ago with the organization of the International Summit on OPV Stability (ISOS), which led to a series of recommended practices.[36] These practices are a good starting point for perovskite cell or mini-module stability studies, although there is work toward establishing an updated version of recommended practices for perovskite solar cells, as even the way in which performance information (e.g., MPP tracking and I-V sweep conditions) is obtained may influence stability. PeLEDs also should have the standard of lifetime measurement under encapsulation like OLEDs in terms of brightness, decay level, measurement environments such as humidity and temperature, and acceleration factors. However, currently it is rather an early stage to address this issue, because the lifetime is too short (<100 h @ 100 nit for high-efficiency devices reported recently).[11,12] More details about the specific goals of stability studies at the materials, cell-, and module-levels, as well as some recommended standardized stability test conditions, can be found elsewhere.[106]

SUPPLEMENTAL INFORMATION

Supplemental Information can be found online at https://doi.org/10.1016/j.joule.2020.04.007.

AUTHOR CONTRIBUTIONS

S.-H.J., J.P., T.-H.H., M.O.R., and K.Z. co-wrote the initial manuscript about optoelectronic measurements of solar cells and light-emitting diodes. T.-H.H. and J.S.K. helped conduct experiments for characterizing electroluminescence efficiency of perovskite light-emitting diodes. F.Z. conducted experiments to characterize perovskite solar cells. T.-W.L. proposed the topic, and T.-H.H., K.Z., M.O.R., S.Y., and T.-W.L. revised the manuscript. All authors contributed to the discussion and revision of the manuscript. S.-H.J., J.P., and T.-H.H. contributed equally to this work.

REFERENCES

1. De Wolf, S., Holovsky, J., Moon, S.J., Löper, P., Niesen, B., Ledinsky, M., Haug, F.-J., Yum, J.-H., and Ballif, C. (2014). Organometallic halide perovskites: Sharp optical absorption edge and its relation to photovoltaic performance. J. Phys. Chem. Lett. *5*, 1035–1039.

2. Xiao, Z., and Yan, Y. (2017). Progress in Theoretical Study of Metal Halide Perovskite Solar Cell Materials. Adv. Energy Mater. *7*, 1701136.

3. Sze, S.M., and Irvin, J.C. (1968). Resistivity, mobility and impurity levels in GaAs, Ge, and Si at 300°K. Solid-State Electron. *11*, 599–602.

4. Frisk, C., Platzer-Björkman, C., Olsson, J., Szaniawski, P., Wätjen, J.T., Fjällström, V., Salome, P., and Edoff, E. (2014). Optimizing Ga-profiles for highly efficient Cu(In, Ga) Se2thin film solar cells in simple and complex defect models. J. Phys. D Appl. Phys. *47*, 485104.

5. Yin, W.-J., Shi, T., and Yan, Y. (2015). Superior Photovoltaic Properties of Lead Halide Perovskites: Insights from First-Principles Theory. J. Phys. Chem. C *119*, 5253–5264.

6. Tan, Z.-K., Moghaddam, R.S., Lai, M.L., Docampo, P., Higler, R., Deschler, F., Price, M., Sadhanala, A., Pazos, L.M., Credgington, D., et al. (2014). Bright light-emitting diodes based on organometal halide perovskite. Nat. Nanotechnol. *9*, 687–692.

7. Kim, Y.H., Cho, H., Heo, J.H., Kim, T.S., Myoung, N., Lee, C.L., Im, S.H., and Lee, T.W. (2015). Multicolored organic/inorganic hybrid perovskite light-emitting diodes. Adv. Mater. *27*, 1248–1254.

8. de Jong, M., Seijo, L., Meijerink, A., and Rabouw, F.T. (2015). Resolving the ambiguity in the relation between Stokes shift and Huang-Rhys parameter. Phys. Chem. Chem. Phys. *17*, 16959–16969.

9. Scholz, R., Gisslén, L., Himcinschi, C., Vragović, I., Calzado, E.M., Louis, E., San Fabián Maroto, E., and Díaz-García, M.A. (2009). Asymmetry between absorption and photoluminescence line shapes of TPD: spectroscopic fingerprint of the twisted biphenyl core. J. Phys. Chem. A *113*, 315–324.

10. Wolf, C., and Lee, T.-W. (2018). Exciton and lattice dynamics in low-temperature processable CsPbBr3 thin-films. Mater. Today Energy *7*, 199–207.

11. Zhao, B., Bai, S., Kim, V., Lamboll, R., Shivanna, R., Auras, F., Ricther, J.M., Yang, L., Dai, M., Alsari, M., et al. (2018). High-efficiency perovskite–polymer bulk heterostructure light-emitting diodes. Nat. Photonics *12*, 783–789.

12. Lin, K., Xing, J., Quan, L.N., de Arquer, F.P.G., Gong, X., Lu, J., Xie, L., Zhao, W., Zhang, D., Yan, C., et al. (2018). Perovskite light-emitting diodes with external quantum efficiency exceeding 20 per cent. Nature *562*, 245–248.

13. Chiba, T., Hayashi, Y., Ebe, H., Hoshi, K., Sato, J., Sato, S., Pu, Y.-J., Ohisa, S., and Kido, J. (2018). Anion-exchange red perovskite quantum dots with ammonium iodine salts for highly efficient light-emitting devices. Nat. Photonics *12*, 681–687.

14. Green, M.A., Hishikawa, Y., Dunlop, E.D., Levi, D.H., Hohl-Ebinger, J., Yoshita, M., and Ho-Baillie, A.W.Y. (2019). Solar cell efficiency tables (Version 54). Progress in Photovoltaics *27*, 565–575. https://www.nrel.gov/pv/assets/images/best-research-cell-efficiencies.20190802.png.

15. IEEE Spectrum. Interactive: Record-Breaking PV Cells. https://spectrum.ieee.org/static/interactive-record-breaking-pv-cells.

16. Forrest, S.R., Bradley, D.D.C., and Thompson, M.E. (2003). Measuring the Efficiency of Organic Light-Emitting Devices. Adv. Mater. *15*, 1043–1048.

17. Xiao, Z., Kerner, R.A., Zhao, L., Tran, N.L., Lee, K.M., Koh, T., Rand, B.P., and Scholes, G.D. (2017). Efficient perovskite light-emitting diodes featuring nanometre-sized crystallites. Nat. Photonics *11*, 108–115.

18. Meng, S.-S., Li, Y.-Q., and Tang, J.-X. (2018). Theoretical perspective to light outcoupling and management in perovskite light-emitting diodes. Org. Electron. *61*, 351–358.

19. Kim, S.-I., Lee, Y., Park, M.-H., Go, G.-T., Kim, Y.-H., Xu, W., Lee, H.D., Kim, H., Seo, D.G., Lee, W., and Lee, T.-W. (2019). Dimensionality Dependent Plasticity in Halide Perovskite Artificial Synapses for Neuromorphic Computing. Adv. Electron. Mater. 1900008, https://doi.org/10.1002/aelm.201900008.

20. Choi, J., Han, J.S., Hong, K., Kim, S.Y., and Jang, H.W. (2018). Organic-Inorganic Hybrid Halide Perovskites for Memories, Transistors, and Artificial Synapses. Adv. Mater. *30*, e1704002.

21. Snaith, H.J., Abate, A., Ball, J.M., Eperon, G.E., Leijtens, T., Noel, N.K., Stranks, S.D., Wang, J.T.W., Wojciechowski, K., and Zhang, W. (2014). Anomalous hysteresis in perovskite solar cells. J. Phys. Chem. Lett. *5*, 1511–1515.

22. Stranks, S.D., and Snaith, H.J. (2015). Metal-halide perovskites for photovoltaic and light-emitting devices. Nat. Nanotechnol. *10*, 391–402.

23. The National Renewable Energy Laboratory (NREL). Reference Solar Spectral Irradiance: Air Mass 1.5. https://rredc.nrel.gov/solar/spectra/am1.5/.

24. PV Lighthouse. Solar Spectrum Calculator. https://www2.pvlighthouse.com.au/calculators/solar_spectrum_calculator/solarspectrumcalculator.aspx.

25. Emery, K., Myers, D., and Rummel, S. (1988). Solar Simulation-Problems and Solutions. Conference Record of the Twentieth IEEE Photovoltaic Specialists Conference *2*, 1087–1091, https://doi.org/10.1109/PVSC.1988.105873.

26. Committee, I.E. (2017). International Electrotechnical Commission 60904-9 Solar Photovoltaic Devices Part 9: Simulator Performance Requirements, Second Edition (IEC Publications).

27. Moriarty, T. (2016). Simple, fast and effective correction for irradiance spatial nonuniformity in measurement of IVs of large area cells at NREL. 2016 IEEE 43rd Photovolt Spec Conf *15*, 1570–1574.

28. Hohl-Ebinger, J., Siefer, G., and Warta, W. (2007). Non-linearity of solar cells in spectral response measurements. 22nd Eur. Photovolt. Sol. Energy Conf. 3–7.

29. Sommeling, P.M., Rieffe, H.C., van Roosmalen, J.A.M., Schönecker, A., Kroon, J.M., Wienke, J.A., and Hinsch, A. (2000). Spectral response and IV-characterization of dye-sensitized nanocrystalline TiO2 solar cells. Sol. Energy Mater. Sol. Cells *62*, 399–410.

30. McMahon, T.J., and Sadlon, K. (1984). Errors in calculated air mass 1 short-circuit currents due to non-linear responsivities. Solar Cells *13*, 99–105.

31. Cowan, S.R., Wang, J., Yi, J., Lee, Y.-J., Olson, D.C., and Hsu, J.W.P. (2013). Intensity and wavelength dependence of bimolecular recombination in P3HT:PCBM solar cells: A white-light biased external quantum efficiency study. J. Appl. Physiol. *113*, 154504.

32. Da, Y., Xuan, Y., and Li, Q. (2018). Quantifying energy losses in planar perovskite solar cells. Sol. Energy Mater. Sol. Cells *174*, 206–213.

33. Fuerst, T.F., Reese, M.O., and Wolden, C.A. (2016). PECVD Synthesis of Flexible Optical Coatings for Renewable Energy Applications. Plasma Process. Polym. *13*, 184–190.

34. Emery, K.A. (2008). Comment on "Roles of donor and acceptor nanodomains in 6% efficient thermally annealed polymer photovoltaics". Appl. Phys. Lett. *92*, 90–91.

35. Reese, M.O., Marshall, A.R., and Rumbles, G. (2018). Reliably Measuring the Performance of Emerging Photovoltaic Solar Cells. In Nanostructured Materials for Type III Photovoltaics (The Royal Society of Chemistry). https://doi.org/10.1039/9781782624585-00001.

36. Reese, M.O., Gevorgyan, S.A., Jørgensen, M., Bundgaard, E., Kurtz, S.R., Ginley, D.S., Olsen, D.C., Llyod, M.T., Morvillo, P., Katz, E.A., et al. (2011). Consensus stability testing protocols for organic photovoltaic materials and devices. Sol. Energy Mater. Sol. Cells *95*, 1253–1267.

37. Kim, M.S., Kang, M.G., Guo, L.J., and Kim, J. (2008). Choice of electrode geometry for accurate measurement of organic photovoltaic cell performance. Appl. Phys. Lett. *92*, 2006–2009.

38. Kiermasch, D., Gil-Escrig, L., Bolink, H.J., and Tvingstedy, K. (2018). Effects of Masking on Open-Circuit Voltage and Fill Factor in Solar Cells (Joule). https://doi.org/10.1016/j.joule.2018.10.016.

39. Kim, D.H., Park, J., Li, Z., Yang, M., Park, J.S., Park, I.J., Kim, J.Y., Berry, J.J., Rumbles, G., and Zhu, K. (2017). 300% Enhancement of Carrier Mobility in Uniaxial-Oriented Perovskite Films Formed by Topotactic-

Oriented Attachment. Adv. Mater. *29*, 1606831.

40. Li, Z., Yang, M., Park, J.S., Wei, S.H., Berry, J.J., and Zhu, K. (2016). Stabilizing Perovskite Structures by Tuning Tolerance Factor: Formation of Formamidinium and Cesium Lead Iodide Solid-State Alloys. Chem. Mater. *28*, 284–292.

41. Sanchez, R.S., Gonzalez-Pedro, V., Lee, J.W., Park, N.G., Kang, Y.S., Mora-Sero, I., and Bisquert, J.; Characteristic Times and Hysteresis (2014). Slow dynamic processes in lead halide perovskite solar cells. Characteristic times and hysteresis. J. Phys. Chem. Lett. *5*, 2357–2363.

42. Unger, E.L., Hoke, E.T., Bailie, C.D., Nguyen, W.H., Bowring, A.R., Heumüller, T., Christoforo, M.G., and McGehee, M.D. (2014). Hysteresis and transient behavior in current-voltage measurements of hybrid-perovskite absorber solar cells. Energy Environ. Sci. *7*, 3690–3698.

43. Shao, Y., Xiao, Z., Bi, C., Yuan, Y., and Huang, J. (2014). Origin and elimination of photocurrent hysteresis by fullerene passivation in CH3NH3PbI3 planar heterojunction solar cells. Nat. Commun. *5*, 5784.

44. Wojciechowski, K., Stranks, S.D., Abate, A., Sadoughi, G., Sadhanala, A., Kopidakis, N., Rumbles, G., Li, C.Z., Friend, R.H., Jen, A.K.Y., and Snaith, H.J. (2014). Heterojunction modification for highly efficient organic-inorganic perovskite solar cells. ACS Nano *8*, 12701–12709.

45. Xiao, Z., Yuan, Y., Shao, Y., Wang, Q., Dong, Q., Bi, C., Sharma, P., Gruverman, A., and Huang, J. (2015). Giant switchable photovoltaic effect in organometal trihalide perovskite devices. Nat. Mater. *14*, 193–198.

46. Tress, W., Marinova, N., Moehl, T., Zakeeruddin, S.M., Nazeeruddin, M.K., and Grätzel, M. (2015). Understanding the rate-dependent J-V hysteresis, slow time component, and aging in CH3NH3PbI3perovskite solar cells: The role of a compensated electric field. Energy Environ. Sci. *8*, 995–1004.

47. Chen, H.W., Sakai, N., Ikegami, M., and Miyasaka, T. (2015). Emergence of hysteresis and transient ferroelectric response in organo-lead halide perovskite solar cells. J. Phys. Chem. Lett. *6*, 164–169.

48. Chen, B., Yang, M., Priya, S., and Zhu, K. (2016). Origin of J-V Hysteresis in Perovskite Solar Cells. J. Phys. Chem. Lett. *7*, 905–917.

49. Contreras-Bernal, L., Ramos-Terrón, S., Riquelme, A., Boix, P.P., Idígoras, J., Mora-Seró, I., and Anta, J.A. (2019). Impedance analysis of perovskite solar cells: a case study. J. Mater. Chem. A Mater. Energy Sustain. *7*, 12191–12200.

50. Pitarch-Tena, D., Ngo, T.T., Vallés-Pelarda, M., Pauporté, T., and Mora-Seró, I. (2018). Impedance spectroscopy measurements in perovskite solar cells: device stability and noise reduction. ACS Energy Lett. *3*, 1044–1048.

51. Park, N.-G., Grätzel, M., Miyasaka, T., Zhu, K., and Emery, K. (2016). Towards stable and commercially available perovskite solar cells. Nat. Energy *1*, 16152.

52. Dunbar, R.B., Duck, B.C., Moriarty, T., Anderson, K.F., Duffy, N.W., Fell, C.J., Kim, J., Ho-Baillie, A., Vak, D., Duong, T., et al. (2017). How reliable are efficiency measurements of perovskite solar cells? the first inter-comparison, between two accredited and eight non-accredited laboratories. Journal of Materials Chemistry *5*, 22542–22558.

53. Khenkin, M.V., Katz, E.A., Abate, A., Bardizza, G., Berry, J.J., Brabec, C., Brunetti, F., Bulovic, V., Burlingame, Q., Carlo, A.D., et al. Consensus Statement for Stability Assessment and Reporting for Perovskite Photovoltaics based on ISOS Procedures. Nat. Energy.

54. BIPM Resolution 3 of the 16th CGPM (1979). http://www.bipm.org/en/CGPM/db/16/3/.

55. Smith, T., and Guild, J. (1931). The c.i.e. colorimetric standards and their use. Transactions of the Optical Society *33*, 73–134.

56. Lee, B.R., Lee, S., Park, J.H., Jung, E.D., Yu, J.C., Nam, Y.S., Heo, J., Kim, J.Y., Kim, B.S., and Song, M.H. (2015). Amine-based interfacial molecules for inverted polymer-based optoelectronic devices. Adv. Mater. *27*, 3553–3559.

57. Chih, Y.K., Wang, J.C., Yang, R.T., Liu, C.C., Chang, Y.C., Fu, Y.S., Lai, W.C., Chen, P., Wen, T.C., Huang, Y.C., et al. (2016). NiO$_x$ Electrode Interlayer and CH$_3$ NH$_2$ /CH$_3$ NH$_3$ PbBr$_3$ Interface Treatment to Markedly Advance Hybrid Perovskite-Based Light-Emitting Diodes. Adv. Mater. *28*, 8687–8694.

58. Meng, F., Zhang, C., Chen, D., Zhu, W., Yip, H.-L., and Su, S.-J. (2017). Combined optimization of emission layer morphology and hole-transport layer for enhanced performance of perovskite light-emitting diodes. J. Mater. Chem. *5*, 6169–6175.

59. Qasim, K., Wang, B., Zhang, Y., Li, P., Wang, Y., Li, S., Lee, S.T., Liao, L.S., Lei, W., and Bao, Q. (2017). Solution-Processed Extremely Efficient Multicolor Perovskite Light-Emitting Diodes Utilizing Doped Electron Transport Layer. Adv. Funct. Mater. *27*, 1606874.

60. Zhang, X., Lin, H., Huang, H., Reckmeier, C., Zhang, Y., Choy, W.C.H., and Rogach, A.L. (2016). Enhancing the Brightness of Cesium Lead Halide Perovskite Nanocrystal Based Green Light-Emitting Devices through the Interface Engineering with Perfluorinated Ionomer. Nano Lett. *16*, 1415–1420.

61. Jeong, S.H., Woo, S.H., Han, T.H., Park, M.H., Cho, H., Kim, Y.H., Cho, H., Kim, H., Yoo, S., and Lee, T.W. (2017). Universal high work function flexible anode for simplified ITO-free organic and perovskite light-emitting diodes with ultra-high efficiency. NPG Asia Mater. *9*, e411.

62. Seo, H.-K., Kim, H., Lee, J., Park, M.-H., Jeong, S.-H., Kim, Y.-H., Kwon, S.-J., Han, T.-H., Yoo, S., and Lee, T.-W. (2017). Efficient Flexible Organic/Inorganic Hybrid Perovskite Light-Emitting Diodes Based on Graphene Anode. Adv. Mater. *29*, 1605587.

63. Cho, H., Jeong, S.-H., Park, M.-H., Kim, Y.-H., Wolf, C., Lee, C.-L., Heo, J.H., Sadhanala, A.,

Myoung, N.S., Yoo, S., Im, S.H., et al. (2015). Overcoming the electroluminescence efficiency limitations of perovskite light-emitting diodes. Science *350*, 1222–1225.

64. Li, G., Rivarola, F.W.R., Davis, N.J.L.K., Bai, S., Jellicoe, T.C., de la Peña, F., Hou, S., Ducati, C., Gao, F., Friend, R.H., et al. (2016). Highly Efficient Perovskite Nanocrystal Light-Emitting Diodes Enabled by a Universal Crosslinking Method. Adv. Mater. *28*, 3528–3534.

65. Kumar, P., Zhao, B., Friend, R.H., Sadhanala, A., and Narayan, K.S. (2017). Kinetic Control of Perovskite Thin-Film Morphology and Application in Printable Light-Emitting Diodes. ACS Energy Lett. *2*, 81–87.

66. Lee, J.W., Choi, Y.J., Yang, J.M., Ham, S., Jeon, S.K., Lee, J.Y., Song, Y.-H., Ji, E.K., Yoon, D.-H., Seo, S., et al. (2017). In-Situ Formed Type I Nanocrystalline Perovskite Film for Highly Efficient Light-Emitting Diode. ACS Nano *11*, 3311–3319.

67. Zhang, X., Sun, C., Zhang, Y., Wu, H., Ji, C., Chuai, Y., Wang, P., Wen, S., Zhang, C., and Yu, W.W. (2016). Bright Perovskite Nanocrystal Films for Efficient Light-Emitting Devices. J. Phys. Chem. Lett. *7*, 4602–4610.

68. Ng, Y.F., Jamaludin, N.F., Yantara, N., Li, M., Irukuvarjula, V.K.R., Demir, H.V., Sum, T.C., Mhaisalkar, S., and Mathews, N. (2017). Rapid Crystallization of All-Inorganic CsPbBr$_3$ Perovskite for High-Brightness Light-Emitting Diodes. ACS Omega *2*, 2757–2764.

69. Cho, H., Wolf, C., Kim, J.S., Yun, H.J., Bae, J.S., Kim, H., Heo, J.M., Ahn, S., and Lee, T.-W. (2017). High-Efficiency Solution-Processed Inorganic Metal Halide Perovskite Light-Emitting Diodes. Adv. Mater. *29*, 1700579.

70. Yu, J.C., Kim, D.W., Kim, B., Jung, E.D., Park, J.H., Lee, A.Y., Lee, B.R., Di Nuzzo, D., Friend, R.H., and Song, M.H. (2016). Improving the Stability and Performance of Perovskite Light-Emitting Diodes by Thermal Annealing Treatment. Adv. Mater. *28*, 6906–6913.

71. Meng, L., Yao, E.P., Hong, Z., Chen, H., Sun, P., Yang, Z., Li, G., and Yang, Y. (2017). Pure Formamidinium-Based Perovskite Light-Emitting Diodes with High Efficiency and Low Driving Voltage. Adv. Mater. *29*, 1603826.

72. Zhao, X., Zhang, B., Zhao, R., Yao, B., Liu, X., Liu, J., and Xie, Z. (2016). Simple and Efficient Green-Light-Emitting Diodes Based on Thin Organolead Bromide Perovskite Films via Tuning Precursor Ratios and Postannealing Temperature. J. Phys. Chem. Lett. *7*, 4259–4266.

73. Yang, X., Zhang, X., Deng, J., Chu, Z., Jiang, Q., Meng, J., Wang, P., Zhang, L., Yin, Z., and You, J. (2018). Efficient green light-emitting diodes based on quasi-two-dimensional composition and phase engineered perovskite with surface passivation. Nat. Commun. *9*, 570.

74. Chen, P., Xiong, Z., Wu, X., Shao, M., Ma, X., Xiong, Z.H., and Gao, C. (2017). Highly Efficient Perovskite Light-Emitting Diodes Incorporating Full Film Coverage and Bipolar Charge Injection. J. Phys. Chem. Lett. *8*, 1810–1818.

75. Bade, S.G.R., Shan, X., Hoang, P.T., Li, J., Geske, T., Cai, L., Pei, Q., Wang, C., and Yu, Z. (2017). Stretchable Light-Emitting Diodes with Organometal-Halide-Perovskite-Polymer Composite Emitters. Adv. Mater. *29*, 1607053.

76. Zhao, L., Yeh, Y.-W., Tran, N.L., Wu, F., Xiao, Z., Kerner, R.A., Lin, Y.L., Scholes, G.D., Yao, N., and Rand, B.P. (2017). *In Situ* Preparation of Metal Halide Perovskite Nanocrystal Thin Films for Improved Light-Emitting Devices. ACS Nano *11*, 3957–3964.

77. Lee, S., Park, J.H., Nam, Y.S., Lee, B.R., Zhao, B., Di Nuzzo, D., Jung, E.D., Jeon, H., Kim, J.Y., Jeong, H.Y., et al. (2018). Growth of Nanosized Single Crystals for Efficient Perovskite Light-Emitting Diodes. ACS Nano *12*, 3417–3423.

78. Ling, Y., Tian, Y., Wang, X., Wang, J.C., Knox, J.M., Perez-Orive, F., Du, Y., Tan, L., Hanson, K., Ma, B., and Gao, H. (2016). Enhanced Optical and Electrical Properties of Polymer-Assisted All-Inorganic Perovskites for Light-Emitting Diodes. Adv. Mater. *28*, 8983–8989.

79. Li, J., Shan, X., Bade, S.G.R., Geske, T., Jiang, Q., Yang, X., and Yu, Z. (2016). Single-Layer Halide Perovskite Light-Emitting Diodes with Sub-Band Gap Turn-On Voltage and High Brightness. J. Phys. Chem. Lett. *7*, 4059–4066.

80. Wu, C., Zou, Y., Wu, T., Ban, M., Pecunia, V., Han, Y., Liu, Q., Song, T., Duhm, S., and Sun, B. (2017). Improved Performance and Stability of All-Inorganic Perovskite Light-Emitting Diodes by Antisolvent Vapor Treatment. Adv. Funct. Mater. *27*, 1700338.

81. Cao, W., Liu, P., Chen, W., Wang, W., Xu, B., Wu, D., Hao, J., Cao, W., Fang, F., Li, Y., et al. (2017). Halide-Rich Synthesized Cesium Lead Bromide Perovskite Nanocrystals for Light-Emitting Diodes with Improved Performance. Chem. Mater. *29*, 5168–5173.

82. Chin, X.Y., Perumal, A., Bruno, A., Yantara, N., Veldhuis, S., Martinez-Sarti, L., Chandran, B., Chirvony, V., Lo, A.S.Z., So, J., et al. (2018). Self-assembled Hierarchical Nanostructured Perovskites Enable Highly Efficient LEDs via Energy Cascade. Energy Environ. Sci. *11*.

83. Kim, Y.-H., Wolf, C., Kim, Y.-T., Cho, H., Kwon, W., Do, S., Sadhanala, A., Park, C.G., Rhee, S.W., Im, S.H., et al. (2017). Highly Efficient Light-Emitting Diodes of Colloidal Metal-Halide Perovskite Nanocrystals beyond Quantum Size. ACS Nano *11*, 6586–6593.

84. Zhao, F., Chen, D., Chang, S., Huang, H., Tong, K., Xiao, C., Chou, S., Zhong, H., and Pei, Q. (2017). Highly flexible organometal halide perovskite quantum dot based light-emitting diodes on a silver nanowire–polymer composite electrode. J. Mater. Chem. *5*, 531–538.

85. Kumar, S., Jagielski, J., Kallikounis, N., Kim, Y.H., Wolf, C., Jenny, F., Tian, T., Hofer, C.J., Chiu, Y.C., Stark, W.J., et al. (2017). Ultrapure Green Light-Emitting Diodes Using Two-Dimensional Formamidinium Perovskites: Achieving Recommendation 2020 Color Coordinates. Nano Lett. *17*, 5277–5284.

86. Deng, W., Xu, X., Zhang, X., Zhang, Y., Jin, X., Wang, L., Lee, S.T., and Jie, J. (2016). Organometal Halide Perovskite Quantum Dot Light-Emitting Diodes. Adv. Funct. Mater. *26*, 4797–4802.

87. Song, J., Li, J., Li, X., Xu, L., Dong, Y., and Zeng, H. (2015). Quantum Dot Light-Emitting Diodes Based on Inorganic Perovskite Cesium Lead Halides (CsPbX3). Adv. Mater. *27*, 7162–7167.

88. Zhang, X., Xu, B., Zhang, J., Gao, Y., Zheng, Y., Wang, K., and Sun, X.W. (2016). All-Inorganic Perovskite Nanocrystals for High-Efficiency Light Emitting Diodes: Dual-Phase CsPbBr3-CsPb2Br5Composites. Adv. Funct. Mater. *26*, 4595–4600.

89. Yassitepe, E., Yang, Z., Voznyy, O., Kim, Y., Walters, G., Castañeda, J.A., Kanjanaboos, P., Yuan, M., Gong, X., Fan, F., et al. (2016). Amine-Free Synthesis of Cesium Lead Halide Perovskite Quantum Dots for Efficient Light-Emitting Diodes. Adv. Funct. Mater. *26*, 8757–8763.

90. Wei, S., Yang, Y., Kang, X., Wang, L., Huang, L., and Pan, D. (2017). Homogeneous Synthesis and Electroluminescence Device of Highly Luminescent CsPbBr₃ Perovskite Nanocrystals. Inorg. Chem. *56*, 2596–2601.

91. Van Le, Q., Park, M., Sohn, W., Jang, H.W., and Kim, S.Y. (2017). Investigation of Energy Levels and Crystal Structures of Cesium Lead Halides and Their Application in Full-Color Light-Emitting Diodes. Adv. Electron. Mater. *3*, 1600448.

92. Tan, Y., Zou, Y., Wu, L., Huang, Q., Yang, D., Chen, M., Ban, M., Wu, C., Wu, T., Bai, S., et al. (2018). Highly Luminescent and Stable Perovskite Nanocrystals with Octylphosphonic Acid as a Ligand for Efficient Light-Emitting Diodes. ACS Appl. Mater. Interfaces *10*, 3784–3792.

93. Koo, W.H., Youn, W., Zhu, P., Li, X.H., Tansu, N., and So, F. (2012). Light extraction of organic light emitting diodes by defective hexagonal-close-packed array. Adv. Funct. Mater. *22*, 3454–3459.

94. Kim, S.Y., and Kim, J.J. (2010). Outcoupling efficiency of organic light emitting diodes and the effect of ITO thickness. Org. Electron. *11*, 1010–1015.

95. Lee, B.R., Jung, E.D., Park, J.S., Nam, Y.S., Min, S.H., Kim, B.S., Lee, K.M., Jeong, J.R., Friend, R.H., Kim, J.S., et al. (2014). Highly efficient inverted polymer light-emitting diodes using surface modifications of ZnO layer. Nat. Commun. *5*, 4840.

96. Kawabata, T., and Ohno, Y. (2013). Optical measurements of OLED panels for lighting applications. J. Mod. Opt. *60*, 1176–1186.

97. Lozuno, A.E., and Alvuwz, J.C. (1997). An Improved Experimental Determination of External Photoluminescence Quantum Efficiency. Adv. Mater. *9*, 230–232.

98. Tanaka, I., and Tokito, S. (2004). Precise Measurement of External Quantum Efficiency of Organic Light-Emitting Devices. Jpn. J. Appl. Phys. *43*, 7733–7736.

99. Dai, X., Zhang, Z., Jin, Y., Niu, Y., Cao, H., Liang, X., Chen, L., Wang, J., and Peng, X. (2014). Solution-processed, high-performance light-emitting diodes based on quantum dots. Nature *515*, 96–99.

100. Wang, N., Cheng, L., Ge, R., Zhang, S., Miao, Y., Zou, W., Yi, C., Sun, Y., Cao, Y., Yang, R., et al. (2016). Perovskite light-emitting diodes based on solution-processed self-organized multiple quantum wells. Nat. Photonics *10*, 699–704.

101. Kim, E., Chung, J., Lee, J., Cho, H., Cho, N.S., and Yoo, S. (2017). A systematic approach to reducing angular color shift in cavity-based organic light-emitting diodes. Org. Electron. *48*, 348–356.

102. Fries, F., Fröbel, M., Ang, P.Y., Lenk, S., and Reineke, S. (2018). Real-time beam shaping without additional optical elements. Light Sci. Appl. *7*, 18.

103. Cho, H., Kim, Y.-H., Wolf, C., Lee, H.-D., and Lee, T.-W. (2018). Improving the Stability of Metal Halide Perovskite Materials and Light-Emitting Diodes. Adv. Mater. *30*, e1704587.

104. Zhao, L., Gao, J., Lin, Y.L., Yeh, Y.-W., Lee, K.M., Yao, N., Loo, Y.-L., and Rand, B.P. (2017). Electrical Stress Influences the Efficiency of CH₃ NH₃ PbI₃ Perovskite Light Emitting Devices. Adv. Mater. *29*, 1605317.

105. Kim, H., Zhao, L., Price, J.S., Grede, A.J., Roh, K., Brigeman, A.N., Lopez, M., Rand, B.P., and Giebink, N.C. (2018). Hybrid perovskite light emitting diodes under intense electrical excitation. Nat. Commun. *9*, 4893.

106. Christians, J.A., Habisreutinger, S.N., Berry, J.J., and Luther, J.M. (2018). Stability in Perovskite Photovoltaics: A Paradigm for Newfangled Technologies. ACS Energy Lett. *3*, 2136–2143.